

Robust Biharmonic Skinning Using Geometric Fields

ANA DODIK, MIT CSAIL, USA

VINCENT SITZMANN, MIT CSAIL, USA

JUSTIN SOLOMON, MIT CSAIL, USA

ODED STEIN, University of Southern California and MIT CSAIL, USA



Fig. 1. Biharmonic skinning weights produced by our method can be used to extrapolate color (top row) or deformations (bottom row) from the control handles into the shape and onto its boundary. Our method computes biharmonic skinning weights on meshes that are typically difficult to handle with standard optimization methods. The SCORPION mesh has been heavily degraded by removing 30% of its faces and randomly perturbing the remaining ones. Our method can compute smooth skinning weights for the BEAVER mesh, created using off-the-shelf 3D scanning software (note: the center of the mesh has been blurred for anonymity). As a result, it contains many thin and self-intersecting triangles, a typical source of errors in finite element solvers. Our method can also be used to deform virtual reality ribbon drawings [Rosales et al. 2019], such as the PIGGYBANK mesh.

Skinning weights are used to rig and deform characters for animation, to compute reduced-order simulations, and to define feature descriptors for geometry processing. Methods built on skinning rely on weight functions that distribute the influence of each degree of freedom across the mesh. *Automatic* skinning methods generate these weight functions with minimal user input, usually by solving a variational problem on a mesh whose boundary is the skinned surface. This formulation necessitates tetrahedralizing the

Authors' addresses: Ana Dodik, anadodik@mit.edu, MIT CSAIL, USA, Cambridge; Vincent Sitzmann, MIT CSAIL, USA, Cambridge; Justin Solomon, MIT CSAIL, USA, Cambridge; Oded Stein, University of Southern California and MIT CSAIL, USA, Los Angeles.

Permission to make digital or hard copies of all or part of this work for personal or classroom use is granted without fee provided that copies are not made or distributed for profit or commercial advantage and that copies bear this notice and the full citation on the first page. Copyrights for components of this work owned by others than ACM must be honored. Abstracting with credit is permitted. To copy otherwise, or republish, to post on servers or to redistribute to lists, requires prior specific permission and/or a fee. Request permissions from permissions@acm.org.

© 2024 Association for Computing Machinery.

0730-0301/2024/6-ART \$15.00

<https://doi.org/10.1145/nnnnnnn.nnnnnnn>

volume bounded by the surface, which brings with it meshing artifacts, the possibility of tetrahedralization failure, and the impossibility of generating weights for surfaces that are not closed. We introduce a *mesh-free* and *robust* automatic skinning method that generates high-quality skinning weights comparable to the current state of the art without volumetric meshes. Our method reliably works even on open surfaces and triangle soups where current methods fail. We achieve this through the use of a Lagrangian representation for skinning weights, which circumvents the need for finite elements while optimizing the biharmonic energy.

CCS Concepts: • **Computing methodologies** → **Mesh geometry models**; **Mesh models**.

Additional Key Words and Phrases: skinning weights, bounded biharmonic weights, neural fields, geometry processing, deformation, partial differential equations, variational problems

ACM Reference Format:

Ana Dodik, Vincent Sitzmann, Justin Solomon, and Oded Stein. 2024. Robust Biharmonic Skinning Using Geometric Fields. *ACM Trans. Graph.* 1, 1 (June 2024), 17 pages. <https://doi.org/10.1145/nnnnnnn.nnnnnnn>

1 INTRODUCTION

The dominant pipeline for computer animation relies on *deformation skeletons*. Skeletons are composed of control handles—typically points and bones—each of which has an associated region of influence on the shape. These regions of influence, referred to as *skinning weights*, specify how deformations of the control handles are to be blended and transferred to the shape.

The simple and intuitive interface of skeletons comes at the cost of having to specify the skinning weights. Modeling tools allow users to specify skinning weights by manually painting them onto the shape, in a slow and painstaking process. To alleviate the challenges of manual skinning weights design, various approaches attempt to automate skinning weight computation. For example, data-driven approaches for this problem rely on 3D deformation data or video (e.g., [Li et al. 2021; Liao et al. 2023]). However, these learning-based methods are class-specific, require an abundance of data, and struggle with out-of-distribution examples.

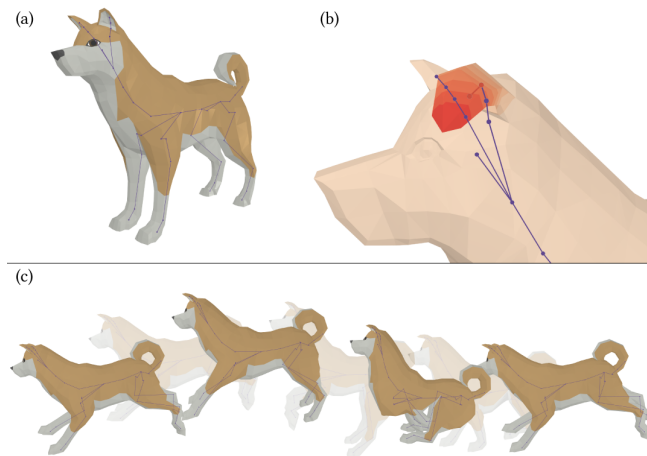


Fig. 2. An illustrative example on the low-poly SHIBA INU mesh, with the skeleton depicted in purple (a). The skinning weight function of the ear bone determines the region of influence of that bone (b). Our method for automatic skinning weight computation produces smooth-looking deformations (c).

An alternative popular approach formulates the computation of automatic skinning weights as an optimization problem with some smoothness objective, side-stepping the need for class-specific data [Baran and Popović 2007; Botsch and Kobbelt 2004; Jacobson et al. 2011, 2012a; Wang et al. 2015; Wang and Solomon 2021].

Optimization-based methods have seen some adoption in commercial software. For example, Pinocchio [Baran and Popović 2007] is implemented in Blender, and bounded biharmonic weights (BBW) [Jacobson et al. 2011] are offered as a tool for 2D animation in Adobe Character Animator. Despite this adoption, manual painting of skinning weights remains predominant. This is, in part, due to **robustness** issues with these methods, as they rely on mesh-based discretizations using the finite-element method (FEM). Famously, FEM-based approaches struggle with “in the wild” data common in geometry processing [Gillespie et al. 2021; Hu et al. 2019; Miller et al.

2023; Sawhney and Crane 2020; Sawhney et al. 2023, 2022; Sharp and Crane 2020a,b; Sharp et al. 2021]. For example, Blender’s implementation raises the error Bone Heat Weighting: Failed to find solution. . . due to issues with FEM, resulting in a plethora of online discussions and tutorials dedicated to cleaning up meshes to avoid this error.

Robustness issues are especially pronounced with methods that necessitate computing a tetrahedral mesh, as fast and robust tetrahedralization remains a challenging open problem [Diazz et al. 2023; Hu et al. 2020, 2018]. This is particularly unfortunate, as the state-of-the-art smoothness-based analytical formulation of skinning weights—bounded biharmonic weights [Jacobson et al. 2011]—necessitates a tetrahedral mesh. Figure 3 demonstrates common a failure case of state-of-the-art fast tetrahedralization software [Hu et al. 2020]. If we want to guarantee that our software can compute a tetrahedral mesh, we either get a fast approximate solution that can lead to visible artifacts, or the tetrahedralization software can take multiple hours only for the downstream FEM solver to fail due to the tetrahedral mesh being too high-resolution.

Recent work suggests that function representations popularized in machine learning and vision show promise as a replacement for FEM and facilitate optimization pipelines for low-level geometry processing problems [Dodik et al. 2023]. However, representations like neural fields [Xie et al. 2022] or Gaussian mixtures [Kerbl et al. 2023] fall short from being directly applicable to problems in geometry processing, such as the automatic optimization of skinning weights. Geometry processing problems come with hard constraints, both those imposed by the geometry of the shape (see Figure 6), as well as constraints imposed by the specific problem formulation (e.g., skinning weights should be non-negative, see Eq. 2). We take inspiration from these approaches, but build in the hard constraints directly into the architecture of the field. Since problems in geometry processing typically have hard constraints on the set of permissible solutions, including e.g. boundary conditions for smoothness energies, we dub these modified differentiable fields *geometric fields*.

In this paper, we introduce a mesh-free, tailor-made representation of skinning weights that satisfies the constraints of the problem by construction. Our representation is guaranteed to satisfy prescribed boundary conditions and constraints associated with skinning weights. While previous work suggests using neural networks, we propose a simpler Lagrangian function representation built on efficient geometric queries. Our representation not only accelerates our method, but importantly respects the constraints imposed by the geometry of the shape, avoiding artifacts like bleeding (see Figure 6). With our architecture, we can optimize the biharmonic energy used to find smooth weights via stochastic gradient descent.

In summary, our main contributions are:

- A robust automatic method for computing skinning weights.
- A Lagrangian representation and approach to solving the bounded biharmonic weights problem without finite elements.
- The use of hardware-accelerated ray tracing for a geometry-aware function parameterization.
- Modifications that allow the method to work on non-watertight domains like triangle soups.
- A thorough qualitative and quantitative investigation of our method.

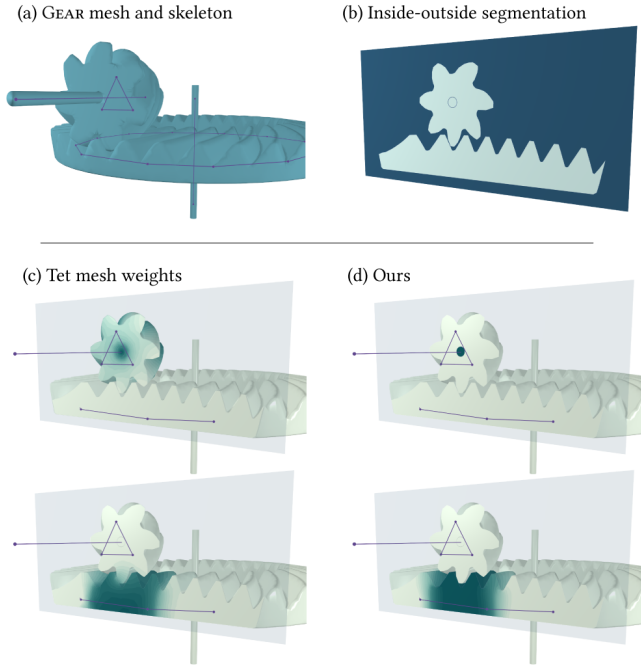


Fig. 3. Our method computes skinning weights inside a volume bounded by a triangle mesh using the formulation proposed by Jacobson et al. [2011], but does away with the need for filling that volume with a tetrahedral mesh. This allows us to compute skinning weights on non-watertight, self-intersecting meshes. We demonstrate the benefits of this approach using the challenging GEAR mesh with its skeleton depicted in purple (a). Since our formulation is volumetric, we show quantities calculated in our algorithm as colors on a planar slice through the volume. In (b), we show the inside-outside segmentation induced by the generalized winding number [Jacobson et al. 2013]. Solving for skinning weights using a tetrahedral mesh from FASTTETWILD [Hu et al. 2020] (with default parameters) results in weights bleeding over boundaries as well as discretization artifacts (c). Modifying FASTTETWILD’s parameters to respect object boundaries increases mesh computation time to 2.52 **hours**, yielding a tetrahedral mesh so large it crashes the MOSEK [ApS 2019] conic solver. In comparison, our weights are smooth, respect object boundaries, and can be computed from the boundary representation in around 5.5 min (d).

2 RELATED WORK

In this section, we mention connections of our work to other methods in the geometry processing literature.

2.1 Robust Geometry Processing

A significant body of prior work has been dedicated to making FEM-based geometry processing more robust. FEM-based algorithms put the burden on the end-user to ensure that 3D meshes are “well-behaved,” requiring the user to e.g. remove self-intersections or to ensure obscure mathematical properties such as manifoldness, watertightness, or boundedness of interior angles. While FEM initially seems like a natural fit for mesh-based data, it is worth noting that

a mesh that is sufficient for representing a shape is not necessarily also a good FEM mesh; moreover, FEM-based methods often require meshing the interior of a volume bounded by a boundary representation, while the latter is sufficient for 3D modeling.

Robust triangle meshing algorithms rely on complex data structures and parallelize poorly [Gillespie et al. 2021; Hu et al. 2019; Sharp and Crane 2020a,b; Sharp et al. 2021], and tetrahedral meshing algorithms all either have strong requirements on the quality of the input (e.g., crashing in the presence of self-intersections) [Diazi et al. 2023; Tournois et al. 2024] or drastically change the appearance of the mesh [Hu et al. 2020, 2018] as in Figure 3. Despite efforts to address mesh-related issues by introducing more meshing tools, these core challenges persist.

To sidestep the issues above, there is emerging interest into mesh-free approaches to geometry processing using Monte Carlo methods [Miller et al. 2023; Sawhney and Crane 2020; Sawhney et al. 2023, 2022]. As of now, this approach to mesh-free geometry processing is not applicable to our setting, as it applies to linear PDE problems rather than the inequality-constrained variational problem needed for skinning. Similarly, geometry processing and physical simulation methods built on the boundary element method (BEM) hold some promise for alleviating dependence on tetrahedralization of a boundary representation, but typical BEM algorithms are restricted to linear PDE, at least in the interior of the domain; this restriction leads BEM-based algorithms in graphics to rely on aggressive relaxations [Solomon et al. 2017] or have to work around limitations of simple physical models like linear elasticity [Sugimoto et al. 2022].

A seminal work in the robust geometry processing literature was the introduction of the generalized winding number [Jacobson et al. 2013]. The generalized winding number allows us to robustly decide whether a point is inside or outside of a given shape. Importantly, it degrades gracefully and produces meaningful results even in the presence of heavily degenerate geometry. Most uses of the generalized winding number for robust geometry processing have been in creating methods for approximate tetrahedral meshing, such as the one used to create Figure 3. In contrast, our method relies on the generalized winding number to modify the optimization objective (see Section 6.3), removing the need for tetrahedralization.

2.2 Automatic Skinning Weights

Our method targets the problem of automatically computing skinning weights given a geometric domain and bones; the mathematical setup of this problem as well as basic uses of skinning weights are outlined in Section 3.

User interfaces for 3D modeling often include means for artists to paint on skinning weights. In an effort to alleviate this largely manual process, automatic skinning weights algorithms use input geometry (e.g., a mesh of a shape that will undergo deformation) and/or example poses to infer the weight functions. This paper focuses on the former setting—by far the most common, since obtaining an exemplary set of poses for a shape that suggest the underlying skinning weights is itself a hard problem. See e.g. [James and Twigg 2005; Kavan et al. 2010; Le and Deng 2012, 2014; Wampler 2016] for examples of data-driven methods in the latter category; we also

mention some neural network architectures that predict skinning weights below.

PDE-based methods. Many classical techniques for automatic skinning weights computation solve a partial differential equation (PDE). Mathematical facts about PDE like the maximum principle and elliptic regularity motivate these models, which consequently inherit properties like smoothness and being a partition of unity.

The best-known PDE methods solve for *harmonic* weights, which satisfy the Laplace equation $\Delta w \equiv 0$ subject to Dirichlet conditions at the bones [Joshi et al. 2007]. These weights are efficient to compute since they are obtained by solving linear systems, but they are only C^0 at the control handles; this property yields unnatural deformations near the handles. The closely-related heat diffusion weights of Baran and Popović [2007] have similar properties; their “Pinocchio” method is implemented in common modeling software including Blender and Maya.

Solving higher-degree PDEs can lead to smoother functions and the possibility of smoothing the weights near control handles; they also can be better posed in higher-dimensions, e.g. volumes in \mathbb{R}^3 as opposed to regions in \mathbb{R}^2 . With these properties in mind, Botsch and Kobbelt [2004] replace the harmonic equation with the biharmonic equation $\Delta^2 w \equiv 0$, and Jacobson et al. [2010]; Tosun [2008] use the triharmonic equation. Although they often remain linear, the main cost of using these methods is the loss of a maximum principle, leading to oscillatory skinning weights.

Variational methods. A class of *variational* methods adds constraints and solves for weights by solving an optimization problem rather than a linear differential equation.

The best-known and widest used method in this class is the *bounded biharmonic weights* (BBW) model [Jacobson et al. 2011]. This method builds on skinning weights algorithms using the biharmonic equation, whose solutions can be characterized as minimizers of the *biharmonic energy* $\int_{\Omega} \|\Delta w\|_2^2 dV$ with constraints only at the boundary. BBW introduces pointwise nonnegativity and partition-of-unity constraints—as well as an implicit Neumann boundary condition [Stein et al. 2018]—leading to a convex quadratic program that can be discretized on a triangle/tetrahedral mesh. This algorithm and its variations provide a gold standard for smooth automatic skinning weights computation, at the cost of efficiency and mesh dependence.

Building on the success of BBW, several works extend the model to improve quality and/or efficiency. For example, Jacobson et al. [2012b] add an extra constraint to ensure that BBWs do not have local extrema. Wang and Solomon [2021] improve efficiency of BBW weights computation by relating the problem to an unconstrained optimization for harmonic weights in a set of metric tensors that parameterize the anisotropic Laplacian; their weights automatically satisfy properties that the BBW model has to add as constraints.

Most variance of BBW rely on a mesh of the domain. To obtain skinning weights for triangle meshes embedded in \mathbb{R}^3 , this means we need a tetrahedralization of the domain bounded by the surface; it is unclear how to extend these methods to non-watertight domains. Jacobson et al. [2013] briefly illustrate how generalized winding numbers—used as a coarse means of distinguishing inside from outside in non-watertight models—can possibly bridge the gap (see

their Figure 20). Our extension to non-watertight domains detailed in Section 6.3 also makes use of Jacobson et al.’s model.

Additional approaches. A zoo of additional geometric methods propose models adjacent to automatic skinning weights computation. For example, Thiery and Eisemann [2018] jointly optimize bone positions and skinning weights using models from elasticity. “Delta mush” methods [Le and Lewis 2019] bypass steps of skinning and weight computation by applying *a posteriori* smoothing to linear-blend skinning deformations using binary binding weights. Bang and Lee [2018] propose a spline-based interface for artists to efficiently create and edit skinning weights.

Dionne and de Lasa [2013, 2014] consider the problem of computing robust skinning weights using a simplistic closed-form formula in terms of distances; they use a variant of Dijkstra’s algorithm to compute distances restricted to the interior of the domain, discretized using a voxel grid. Their method has some robustness to non-watertight edges but requires a dense voxelization in the presence of thin features to avoid bleeding between disconnected parts of the shape; they also do not optimize a smoothness energy, which can yield artifacts at points where shortest-path distance is not differentiable.

Neural representations. The closest-related work to ours is the work of Dodik et al. [2023], which optimizes for generalized barycentric coordinates using a neural representation; see their work for past literature on generalized barycentric coordinates. Although the broad idea of using nonconvex machine learning-inspired function representations for geometry processing also underlies our work, their method is not directly applicable to our problem due to stark differences between problem statements. In particular, building in hard constraints of the function class of barycentric coordinates requires a complicated purpose-built architecture that is unnecessary in our formulation; see Section 5.1 for precise discussion.

Other works use neural networks to predict skinning weights learned from data. These methods are *not* comparable to ours, since they are solving a data-driven problem, although some of their architectures parameterize skinning weights functions in various ways, providing a point of high-level comparison. Similarly to our construction in Section 4.1, these methods commonly use `softmax` and related activation functions to ensure that predicted skinning weights sum to one, but unlike our architecture they rarely enforce other constraints of the problem.

We mention axes along which methods for learning skinning weights vary. A key decision is the architecture and its interaction with the shape representation; for example, many learned skinning weights employ graph neural networks [Liu et al. 2019; Mosella-Montoro and Ruiz-Hidalgo 2022; Pan et al. 2021], while others use convolutional neural networks [Ouyang and Feng 2020] or Gaussian splatting [Kocabas et al. 2023] to represent and process shapes. Another axis is the training data. While many works rely on direct supervision, some infer skinning weights and related quantities from deformations or by jointly optimizing bone positions with skinning weights [Chen et al. 2021; Li et al. 2021; Ma and Zhang 2023; Xu et al. 2020; Yang et al. 2021]; others incorporate modalities like video [Liao et al. 2023]. Jeruzalski et al. [2020]; Kant et al.

[2023] use neural representations to solve inverse skinning problems. A few methods also introduced specialized architectures and loss terms, e.g., for handling interactions between cloth and human bodies [Ma et al. 2022; Wu et al. 2020] or for supporting a larger pipeline to learn articulated 3D animals [Wu et al. 2023]. Beyond Laplacian regularization terms to smooth weights and deformations (see e.g. [Liao et al. 2023]), these papers are primarily concerned with inference of skinning weights from data rather than using neural representations to solve variational problems for geometric skinning weights.

2.3 Physics Informed Neural Networks in Graphics

A recently popular approach for discretization-free PDE solutions on geometric domains employs physics-informed neural networks (PINNs), such as the works of Raissi et al. [2019]; Wang and Solomon [2021]. These are used, e.g., to solve PDEs for physical simulation [Chen et al. 2023], find watertight surfaces from point clouds [Gropp et al. 2020; Sitzmann et al. 2020], and to solve general hyperbolic equations [Rodriguez-Torrado et al. 2021]. Similar to the way we enforce boundary conditions, these networks can be enhanced with explicit boundary constraints [Anonymous 2024; Chen et al. 2024; Lu et al. 2021; Sukumar and Srivastava 2022]. Other approaches for enforcing constraints on PDEs include [Djeumou et al. 2022; Liu et al. 2022; Mohan et al. 2023; Zhong et al. 2023].

3 PRELIMINARIES

Suppose we are given a shape $\mathcal{P} \subset \mathbb{R}^d$ with boundary $\partial\mathcal{P}$ and a skeleton consisting of a set of *control handles* $\mathcal{H} = \{\mathbf{h}_i\}_{1 \leq i \leq K}$. Most commonly, control handles are either point handles ($\mathbf{p}_i \in \mathcal{P}$) or bones/line-segments ($\mathbf{b}_i \in \mathcal{P} \times \mathcal{P}$). Each control handle has an associated *skinning weight function*, $\alpha_i : \mathcal{P} \rightarrow \mathbb{R}^+$, with $\boldsymbol{\alpha}(\mathbf{x}) = [\alpha_1(\mathbf{x}), \dots, \alpha_K(\mathbf{x})]^\top$ denoting the vector-valued skinning weights function.

Skinning is the process of using the skinning weights to extrapolate SE(3) deformations from the control handles onto any point in the domain $\mathbf{x} \in \mathcal{P}$. Two common approaches are Linear Blend Skinning (LBS) [Magenat-Thalmann et al. 1988] and Dual Quaternion Skinning (DQS) [Kavan et al. 2008]:

$$\text{LBS}(\mathbf{x}) := \sum_{i=1}^K \alpha_i(\mathbf{x}) M_i, \quad \text{DQS}(\mathbf{x}) := \frac{\sum_{i=1}^K \alpha_i(\mathbf{x}) \mathbf{q}_i}{\left\| \sum_{i=1}^K \alpha_i(\mathbf{x}) \mathbf{q}_i \right\|}, \quad (1)$$

where M_i is the 4×4 matrix representation of the deformation defined at control handle i , and \mathbf{q}_i is the corresponding deformation represented as a dual quaternion. See [Jacobson et al. 2014] for a comprehensive introduction.

Skinning weights functions satisfy a set of properties at each $\mathbf{x} \in \mathcal{P}$:

- **NON-NEGATIVITY.** A handle cannot have negative influence over a point: $\alpha_i(\mathbf{x}) \geq 0$.
- **PARTITION OF UNITY.** The influence of all handles must sum up to 100%: $\sum_i \alpha_i(\mathbf{x}) = 1$.
- **LAGRANGE PROPERTY.** A handle must have 100% influence over itself: $\alpha_i(\mathbf{h}_j) = \delta_{ij}$.

Many functions $\boldsymbol{\alpha}$ satisfy these constraints, which mathematically define a *partition of unity*. To pick one set of skinning weights functions among the many possible, we typically optimize some objective function.

Following the success of bounded biharmonic weights [Jacobson et al. 2011], we optimize the biharmonic energy under the skinning weight constraints, leading to the following variational problem:

$$\min_{\alpha_{i \in [1, K]}} \sum_{i=1}^K \int_{\mathcal{P}} |\Delta \alpha_i(\mathbf{x})|^2 dV(\mathbf{x}), \quad (2)$$

$$\text{s.t. } \alpha_i(\mathbf{x}) \geq 0, \quad \forall \alpha_i, \mathbf{x} \in \mathcal{P}, \quad (\text{non-negativity}) \quad (2.1)$$

$$\sum_i \alpha_i(\mathbf{x}) = 1, \quad \forall \mathbf{x} \in \mathcal{P}, \quad (\text{partition of unity}) \quad (2.2)$$

$$\alpha_i(\mathbf{h}_j) = \delta_{ij}, \quad \forall \alpha_i, \mathbf{h}_j, \quad (\text{Lagrange property}) \quad (2.3)$$

$$\mathbf{n}_y^\top \nabla \alpha_i(\mathbf{y}) = 0, \quad \forall \alpha_i, \mathbf{y} \in \partial\mathcal{P} \quad (\text{zero Neumann}) \quad (2.4)$$

where δ_{ij} is the Kronecker delta, V is the volume form of \mathcal{P} , and \mathbf{n}_y is the surface normal at the boundary point \mathbf{y} .

Even though (2.4) is not explicitly featured in the original BBW article [Jacobson et al. 2011], that original method nevertheless contains these zero Neumann boundary conditions *implicitly*. Stein et al. [2018] show that the mixed FEM discretization employed in the original BBW method leads to baked-in zero Neumann conditions in the result. In order to reproduce their results, we have decided to include these boundary conditions *explicitly*. This does not mean that zero Neumann are the best boundary conditions for computing automatic skinning weights. Other boundary conditions might be suitable for some applications, although *some* choice of boundary conditions should be made, as the natural boundary conditions of the biharmonic energy (Eq. 2) can lead to excess noise if not enough other constraints are present [Stein et al. 2018, Fig. 3].

4 ROBUST BIHARMONIC SKINNING

With mathematical preliminaries in place, we proceed by explaining the high-level overview of our model before giving specifics of how we enforce the skinning weight constraints in Section 4.1. Looking forward, Section 5 includes the specifics of our Lagrangian function representation. Finally, we address several practical considerations in Section 8.

To design a geometric field for skinning weights functions, we have design it to include the constraints in Equation 2 into the model architecture. At a high level, our model composes a smooth parametric function $\mathcal{N}_\theta : \mathcal{P} \rightarrow \mathbb{R}^K$, which maps every point in the domain to one value per control handle, with a composite *activation function*, which ensures that the output satisfies the skinning weight constraints.

We compute our robust automatic skinning weights in two steps. First, we modify the generic smooth parametric function \mathcal{N}_θ to satisfy all skinning weight constraints except the Neumann boundary conditions, leading to a set of candidate weights $\hat{\boldsymbol{\alpha}}$:

$$\hat{\boldsymbol{\alpha}}(\mathbf{x}) := \Phi_L(\Phi_C \circ \mathcal{N}_\theta(\mathbf{x}), \mathbf{x}). \quad (\text{RBS})$$

Here, Φ_L enforces the Lagrange property and Φ_C enforces the non-negativity and partition of unity properties. We then modify $\hat{\boldsymbol{\alpha}}$ to the

final skinning weights geometric field α by incorporating Neumann conditions. This step is easily implemented but more difficult to describe in the notation above; see discussion in Section 4.2.2. Lastly, we incorporate constraints dictated by the geometry of the object by using a carefully constructed function representation described in Section 5

We next discuss how to construct Φ_C in Section 4.1 and introduce boundary conditions in Section 4.2. We address the specific choice of \mathcal{N}_θ in Section 5.

4.1 Non-negativity and Partition of Unity

We can incorporate the non-negativity and partition of unity constraints using standard machine learning tools. These conditions force the output $\mathcal{N}_\theta(\mathbf{x})$ to parameterize a *categorical probability distribution* over the control handles. Let $\mathbf{f} \in \mathbb{R}^K$ contain the outputs of \mathcal{N}_θ at some point \mathbf{x} . We can satisfy Equations 2.1 and 2.2 by first applying an elementwise `softplus` function—which has the effect of mapping the elements of \mathbf{f} to the non-negative reals—and then normalizing:

$$\Phi_C(\mathbf{f})_i := \frac{\text{softplus}(f_i)}{\sum_{j=1}^K \text{softplus}(f_j)}. \quad (3)$$

Discussion. A more common choice in machine learning would be the exponential function instead of a `softplus`. We found `softplus` to be preferable for several reasons. A normalized exponential acts as a soft maximum function, amplifying the magnitude of the largest output value. However, this behavior is the opposite of what we want, as multiple control handles can exert influence over the same region. More practically, an exponential activation has a larger span of possible gradient values, which yields instabilities during training.

4.2 Enforcing Boundary Conditions

We are now left to implement the Lagrange property and the zero Neumann boundary condition from Equations 2.3 and 2.4. The Lagrange property can be thought of as a Dirichlet boundary condition, leading to similar treatments for both.

Boundary conditions are fundamental for physics-informed neural networks (PINNs). The most common approach to enforcing PINN boundary conditions involves an additional loss term for each boundary condition [Raissi et al. 2019]. In this framework, it remains unclear how the interior and the boundary loss terms should be combined, leading to manual case-by-case parameter tuning and a brittle optimization procedure. As a solution, recent work has introduced ways of enforcing losses as hard constraints by reparameterizing the function [Sukumar and Srivastava 2022]. In our work, we opt for this strategy due to its robustness and build boundary conditions into the model architecture.

In comparison to previous work [Sukumar and Srivastava 2022; Zhong et al. 2023], our approach fulfills a number of design requirements:

- It does not require a specific shape representation such as a signed distance field, nor does it impose restrictions on the topology of the boundary; we require only closest-point queries.

- We only reparameterize the function in an ε -neighborhood of the boundary. This means that the majority of the computation remains unmodified, reducing overhead.
- Our reparameterization only requires access to function values and not gradients, even when enforcing zero Neumann boundary conditions. This again reduces the necessary computation and avoids the need for fourth-order derivatives.

4.2.1 Lagrange property. Equation 2.3 states that a control handle \mathbf{h}_i should have complete influence over itself. We begin by restating Equation 2.3 in terms of a control handle indicator function, $\mathbf{e} : \mathcal{P} \rightarrow \{0, 1\}^K$. We define \mathbf{e} such that, for all \mathbf{x} that lay on handle \mathbf{h}_i , the i^{th} element of $\mathbf{e}(\mathbf{x})$ equals 1 and all other elements equal 0:

$$\mathbf{e}_i(\mathbf{x}) := \begin{cases} 1 & \text{if } \mathbf{x} \in \mathbf{h}_i, \\ 0 & \text{otherwise.} \end{cases} \quad (4)$$

It follows that the Lagrange condition can be expressed as in terms of \mathbf{e} as

$$\hat{\alpha}(\mathbf{x}) = \mathbf{e}(\mathbf{x}), \quad \forall \mathbf{x} \in \mathbf{h}_{i \in [1, K]}. \quad (5)$$

To enforce this boundary condition, we construct a mollified version of \mathbf{e} —denoted as $\tilde{\mathbf{e}}$ —that equals \mathbf{e} on the control handles and quickly falls off to zero as we move away. Then, we can differentially interpolate between $\Phi_C \circ \mathcal{N}_\theta(\mathbf{x})$ and $\mathbf{e}(\mathbf{x})$ as \mathbf{x} approaches a control handle.

Formally, if a point \mathbf{x} is inside of a tubular ε -neighborhood of any handle \mathbf{h}_i , we use its distance to \mathbf{h}_i to interpolate between $\Phi_C \circ \mathcal{N}_\theta(\mathbf{x})$ and $\tilde{\mathbf{e}}$:

$$\hat{\alpha}(\mathbf{x}) := \tilde{\mathbf{e}}(\mathbf{x}) + \left(1 - \sum_{i=1}^K \tilde{\mathbf{e}}_i(\mathbf{x})\right) \Phi_C \circ \mathcal{N}_\theta(\mathbf{x}). \quad (6)$$

The right-hand side of this expression defines $\Phi_L(\mathbf{f}, \mathbf{x})$ in (RBS) by equating $\mathbf{f} \cong \Phi_C \circ \mathcal{N}_\theta(\mathbf{x})$.

We must choose $\tilde{\mathbf{e}}$ carefully such that the properties in Equation 2.1 and 2.2 are conserved. Moreover, we must take into account that the ε -neighborhoods of two or more handles often overlap, e.g., because bone handles often have shared vertices. To this end, we introduce the following mollifiers:

$$\begin{aligned} \mathbf{b}_i(\mathbf{x}) &:= 1 - \text{smoothstep}\left(\frac{d(\mathbf{x}, \mathbf{h}_i)^2}{\varepsilon^2}\right) \\ \bar{\mathbf{b}}(\mathbf{x}) &:= 1 - \min_{i \in [1, K]} \left\{ \text{smoothstep}\left(\frac{d(\mathbf{x}, \mathbf{h}_i)^2}{\varepsilon^2}\right) \right\}. \end{aligned} \quad (7)$$

In this construction, \mathbf{b}_i represents a bump function around handle i , $\bar{\mathbf{b}}$ represents a scalar bump function around all of the handles, and $d(\mathbf{x}, \mathbf{h}_i)$ is a distance function

$$d(\mathbf{x}, \mathbf{h}_i) = \begin{cases} \|\mathbf{x} - \mathbf{h}_i\|_2, & \text{if } \mathbf{h}_i \text{ is a point handle} \\ \|\mathbf{x} - \text{proj}_{\mathbf{h}_i}(\mathbf{x})\|_2 & \text{if } \mathbf{h}_i \text{ is a bone handle,} \end{cases} \quad (8)$$

where $\text{proj}_{\mathbf{h}_i}$ represents the closest-point projection of \mathbf{x} onto \mathbf{h}_i . However, $\bar{\mathbf{b}}$ does not yet respect the partition of unity constraint, and therefore we introduce one last modification:

$$\tilde{\mathbf{e}}_i(\mathbf{x}) := \frac{\mathbf{b}_i(\mathbf{x})}{\sum_{j=1}^K \mathbf{b}_j(\mathbf{x})}. \quad (9)$$

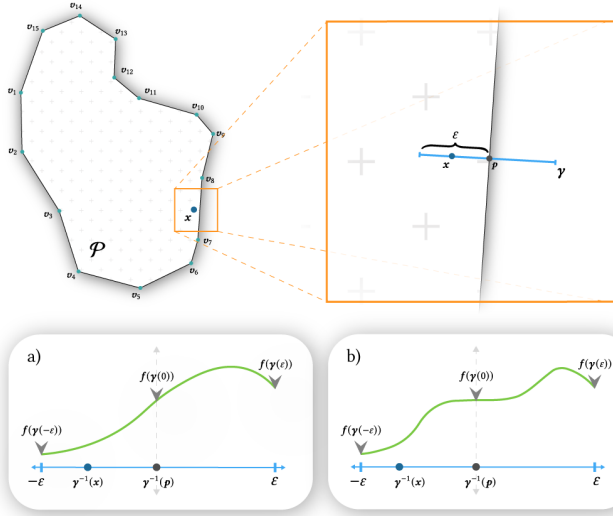


Fig. 4. An illustration of our zero Neumann reparameterization. For any point x in an ε -neighborhood of the boundary, we first find the closest boundary point, $y \in \partial\mathcal{P}$.

Intuitively, we first normalize the individual handle mollifiers to ensure that they respect the partition of unity property. Since all individual handle mollifiers are zero away from the handles, this normalization introduces discontinuities. To combat this, we multiply everything by a joint bump function based on the distance to the closest handle.

4.2.2 Zero Neumann boundary conditions. We modify $\hat{\alpha}$ near the boundary to enforce the zero Neumann boundary condition (2.4). Given $x \in \mathcal{P}$ where we wish to evaluate $\alpha(x)$, we first find the closest boundary point $y \in \partial\mathcal{P}$. We will refer to the distance between x and y as t and to the surface normal at y as n_y . Our goal is to edit $\hat{\alpha}$ to obtain α with the property that, as $t \rightarrow 0$, we have $(\alpha(x) - \alpha(y))/t \rightarrow 0$.

As there are many ways to design this procedure, we opt to preserve as much of the original function as possible, i.e., we design α so that $\alpha(x) = \hat{\alpha}(x)$ for all x outside a ε neighborhood of $\partial\mathcal{P}$.

We begin by defining a parametric line, $\gamma : [-\varepsilon, \varepsilon] \rightarrow \mathcal{P}$, that connects x and y , satisfying $\gamma(0) = y$, $\gamma(t) = x$, and $\gamma' \equiv n_y$. This allows us to rewrite the boundary condition as

$$\left. \frac{d}{dt} \alpha(\gamma(t)) \right|_{t=0} = n_y \cdot \nabla \alpha(y) = 0. \quad (10)$$

To satisfy this condition, we write

$$\alpha(x) := \hat{\alpha}(x) + w_N(t)(\hat{\alpha}(y) - \hat{\alpha}(x)), \quad (11)$$

where $w_N[0, \varepsilon] \rightarrow [0, 1]$ is an interpolant function with $w_N(0) = 1$, $w_N(\varepsilon) = 0$, and $w'_N(0) = 0$. We use a smoothstep function for the interpolant: $w_N(t) = \text{smoothstep}(\frac{t}{\varepsilon})$. The entire formulation is illustrated in Figure 4.

By construction, α satisfies the following property:

PROPOSITION 4.1. α satisfies zero Neumann conditions for any smooth $\hat{\alpha}$ on the interiors of the boundary facets of \mathcal{P} .

PROOF. We need to check the property $n_y \cdot \nabla \alpha(y) = 0$. By the chain rule,

$$\begin{aligned} n_y \cdot \nabla \alpha(y) &= n_y \cdot (\nabla \hat{\alpha}(y) + w'_N(0) \underbrace{(\hat{\alpha}(y) - \hat{\alpha}(y))}_{=0} - \underbrace{w_N(0)}_{=1} \nabla \hat{\alpha}(y)) \\ &= n_y \cdot (\nabla \hat{\alpha}(y) - \nabla \hat{\alpha}(y)) = 0. \end{aligned}$$

In the first equality, note that the term next to $w'_N(0)$ contains only a single derivative of $\hat{\alpha}$; the other term vanishes since we are projecting onto the flat boundary facets of \mathcal{P} . \square

The proposition above has to be stated carefully because polygonal choices of \mathcal{P} necessarily have sharp corners, where Neumann conditions are ill defined. Empirically, we find that behavior of our model near these corners is still reasonable and converges to the proper global boundary conditions as the boundary is refined.

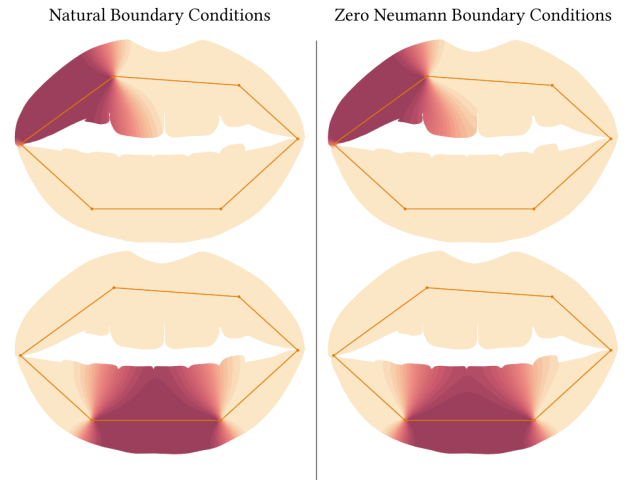


Fig. 5. We demonstrate the effect of our zero Neumann boundary condition constraints; on the right, the isolines of the level-sets are indeed orthogonal to the boundary of the shape, demonstrating the effectiveness of our implementation.

5 FUNCTION REPRESENTATION

Our parameterization of skinning weights functions in Section 4 is built on a generic smooth parametric function, \mathcal{N}_θ . Following previous work like the papers outlined in Section 2, it might be tempting to use a neural network as a plug-and-play function representation. Instead, we propose a faster, more interpretable, and simpler representation inspired by classical computer graphics models as well as modern splat-based methods.

5.1 Kernel-Based Parameterization

Our form for \mathcal{N}_θ is built on a collection of pairs $\mathcal{X} := \{(x_i, f_i)\}_{1 \leq i \leq N}$, where $x_i \in \mathcal{P}$ is a point in the domain and $f_i \in \mathbb{R}^K$ is a feature vector stored at that point. The points x_i are sampled uniformly

from the domain \mathcal{P} and fixed constants; the variables when optimizing for skinning weights functions are the feature vectors f_i . See Section 8 for details on how the x_i 's are sampled.

Evaluated at a point $\mathbf{x} \in \mathcal{P}$, we take

$$\mathcal{N}_\theta(\mathbf{x}) := \frac{\sum_{i=1}^N k(\mathbf{x}, \mathbf{x}_i) f_i}{\sum_{i=1}^N k(\mathbf{x}, \mathbf{x}_i)}, \quad (12)$$

where $k(\mathbf{x}, \mathbf{y})$ is an affinity kernel between \mathbf{x} and \mathbf{y} .

This form for \mathcal{N}_θ is built on classical methods for kernel regression [Nadaraya 1964; Watson 1964] and is a common tool in computer graphics, ranging from point cloud processing [Alexa et al. 2004; Coifman and Lafon 2006; Pauly et al. 2003] to simulation [Gingold and Monaghan 1977; Lucy 1977]. It is less commonly used in geometry processing due to difficulties in enforcing boundary conditions and incorporating geometric information of the underlying domain, as well as to historic limitations of hardware and optimization algorithms. Modern machine learning techniques and advances in GPU hardware, however, make this a viable representation for variational problems.

We opt for this kernelized form over a neural network for a multitude of reasons. Skinning weights functions tend to be smooth and well-approximated by samples on a point cloud. Moreover, in Section 5.2, we propose a kernel k that incorporates structural information and prevents *bleeding* artifacts over the boundaries of the shape. This effect would be non-trivial to accomplish using a neural network. Lastly, this form for \mathcal{N}_θ localizes the degrees of freedom on the domain of the problem, making it possible to visualize and reason about design parameters as shown in Sections 8 and 9.

REMARK (BARYCENTRIC COORDINATES). *Dodik et al.'s work on barycentric coordinates [2023] provides an interesting point of contrast to our own on skinning weights. The skinning weights problem is closely linked to our Equation 2, with one additional "reproduction" constraint. This additional constraint, however, motivates their function parameterization, which is built by sampling simplices in the domain and combining their linear barycentric coordinate functions. Thanks to the missing reproduction constraint, our parameterization is much simpler and does not scale cubically in the size of the domain.*

5.2 Visibility-based Kernel

A standard affinity kernel is the exponential kernel [Coifman and Lafon 2006; Nadaraya 1964; Watson 1964]:

$$k_E(\mathbf{x}, \mathbf{y}) = \exp\left\{-\frac{1}{2\sigma^2}\|\mathbf{x} - \mathbf{y}\|^2\right\}, \quad (13)$$

where σ governs the *spread* of the kernel. However, as this kernel is based on the extrinsic distance between \mathbf{x} and \mathbf{y} , it can lead to *bleeding* artifacts demonstrated in Figure 6.

Previous work [Jacobson et al. 2011, 2012a; Wang and Solomon 2021] avoids bleeding by meshing the interior of \mathcal{P} and associating degrees of freedom and objective terms with elements of the mesh. Reliance on a conforming mesh of the domain (e.g., the volume bounded by an animated character's outer surface) with sufficient quality to discretize and solve skinning weights problems hampers the efficiency and reliability of automatic skinning weights computation, since design of fast and robust meshing algorithms

remains challenging [Diazi et al. 2023; Hu et al. 2020, 2018]. Moreover, this limitation prevents computation of skinning weights on triangle soups and other potentially disconnected domains, as we consider in Section 6.3.

To address bleeding using GPU-friendly queries without a volume mesh, we modify the kernel k to only allow for pairs of points if they are *visible* to each other:

$$k_{RT}(\mathbf{x}, \mathbf{y}) = \mathcal{V}(\mathbf{x} \leftrightarrow \mathbf{y}) \exp\left\{-\frac{1}{2\sigma^2}\|\mathbf{x} - \mathbf{y}\|^2\right\}. \quad (14)$$

Here, $\mathcal{V}(\mathbf{x} \leftrightarrow \mathbf{y})$ is a visibility indicator function between \mathbf{x} and \mathbf{y} , defined as 0 if the distance from \mathbf{x} to the nearest intersection towards \mathbf{y} is smaller than the distance between \mathbf{x} and \mathbf{y} , and as 1 otherwise. This construction is illustrated visually in Figure 7.

In practice, checking visibility distills down to a ray-mesh intersection query. Efficient, robust algorithms support this query [Pharr et al. 2016, Chapter 6.8], which recently have also become computationally feasible for our application with the recent advent of hardware-accelerated ray tracing [Parker et al. 2010]. As a point of reference, a similar approach has been proposed to interpolate irradiance caches in real-time rendering [Halen and Hayward 2021; Majercik et al. 2019].

To enable fast GPU radius queries, we truncate the kernel after a distance $r = 3\sigma$ and use a hash-grid data structure. To further reduce computational cost, we default to k_E if the closest boundary point to \mathbf{x} is a distance larger than r away from \mathbf{x} , doing away with the need for ray-tracing. Note that we have already computed the closest boundary point for the zero Neumann conditions in Section 4.1, requiring no additional computation for this optimization.

Therefore, for a given query point \mathbf{x} and point cloud point $\mathbf{x}_i \in \mathcal{X}$ the final composite kernel used by our model is given by

$$k(\mathbf{x}, \mathbf{x}_i) = \begin{cases} k_{RT}(\mathbf{x}, \mathbf{x}_i) & \text{if } d(\mathbf{x}, \partial\mathcal{P}) < r \\ k_E(\mathbf{x}, \mathbf{x}_i) & \text{otherwise,} \end{cases} \quad (15)$$

where $d(\mathbf{x}, \partial\mathcal{P})$ denotes the distance of \mathbf{x} to the boundary of \mathcal{P} .

In Section 6, we use a similar strategy to estimate smoothness energies while respecting the interior structure of the domain.

6 OBJECTIVE FUNCTION

With our representation of skinning weights functions in place, we proceed to describe our methods for computing and optimizing the biharmonic energy, the smoothness energy we use as an objective function in (2). Our approach uses a randomized estimator compatible with stochastic gradient-based optimization techniques.

6.1 Estimation and Optimization of Biharmonic Energy

In each training iteration, we uniformly randomly sample $M = 2^{15}$ samples $\{\mathbf{y}_j\}_{j=1}^M$ in the interior of the domain \mathcal{P} , used as quadrature points to compute our approximation of the biharmonic energy objective. If a mesh of the interior is available, we use it for random sampling of the interior; this mesh is used only for sampling and does *not* have to satisfy the quality conditions that are typically necessary for FEM. If a mesh is unavailable, we randomly sample the ambient space and use the generalized winding number [Jacobson

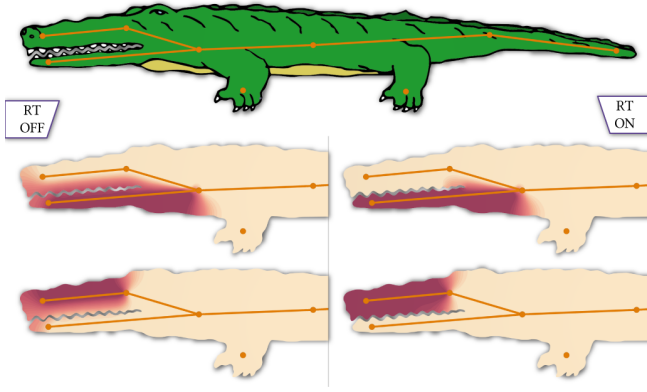


Fig. 6. We demonstrate the effects of our visibility-aware kernel on the CROCODILE mesh. On the left, skinning weights optimized using k_E exhibit undesirable *bleeding artifacts*. On the right, we can see that optimizing for skinning weights using k_{RT} mitigates the issue.

et al. 2013] to reject samples below a threshold, as described below in Section 6.3.

Given our set of samples, we use a Monte Carlo estimate of the bilaplacian energy in Equation 2:

$$\sum_{i=1}^K \int_{\mathcal{P}} |\Delta \alpha_i(\mathbf{y})|^2 dV(\mathbf{y}) \approx \frac{V(\mathcal{P})}{M} \sum_{i=1}^K \sum_{j=1}^M |\hat{\Delta} \alpha_i(\mathbf{y}_j)|^2, \quad (16)$$

where $\hat{\Delta}$ is a visibility-aware finite-difference Laplacian estimator defined next in Section 6.2.

We optimize this objective using the Adam optimizer [Kingma and Ba 2014]. A new set of samples \mathbf{y}_j is drawn in each iteration of Adam. Note Wang and Solomon [2021] also find Adam to be an effective optimizer for skinning weights problems.

6.2 Finite Differences

Previous work highlights problems in relying on automatic differentiation to compute higher-order derivatives of function representations like ours [Chetan et al. 2023; Li et al. 2023]; in particular, differential quantities obtained through automatic differentiation tend to be noisy, and using them for optimization results in visible artifacts [Chetan et al. 2023]. On the other hand, a naïve finite-difference estimator can yield bleeding artifacts similar to those in Figure 6. Here, we suggest a stochastic estimator of the Laplacian that reduces computation time and avoids bleeding.

A standard finite-difference estimator of the Laplacian, Δ_h can be defined as

$$\Delta_h f(\mathbf{y}) = \frac{-2df(\mathbf{y}) + \sum_{i=1}^d (f(\mathbf{y} + h\mathbf{e}_i) + f(\mathbf{y} - h\mathbf{e}_i))}{h^2}, \quad (17)$$

where h is the finite-difference step size, and \mathbf{e}_i represents the i^{th} basis vector in \mathbb{R}^d . This well-known finite-difference Laplacian requires a linear number $2d + 1$ of computations in the dimensionality d of the ambient space; this means a single term on the right-hand side of (16) would require 5 evaluations of α_i in 3D ($d = 3$) and 3 evaluations in 2D ($d = 2$).

Instead, since our evaluation of the objective function is stochastic anyway, we use a modified stochastic Laplacian estimator:

$$\hat{\Delta}_h f(\mathbf{y}) = \frac{-2f(\mathbf{y}) + f(\mathbf{y} + h\mathbf{v}) + f(\mathbf{y} - h\mathbf{v})}{h^2}, \quad (18)$$

where \mathbf{v} is uniformly drawn from the unit sphere S^{d-1} ; we draw a different \mathbf{v} for each term in (16). The expectation of this expression over $\mathbf{v} \in S^{d-1}$ converges to Δf as $h \rightarrow 0$. Our expression (18) simultaneously reduces the number of function evaluations to a constant independent of dimension, and it removes the axis alignment bias of the standard estimator (17).

REMARK (BIAS). *There are two sources of minor bias in our estimate (16) relative to the true biharmonic energy on the left-hand side. First, we use a positive step size $h > 0$ rather than limiting $h \rightarrow 0$. Second, by Jensen’s inequality, squaring (18) leads to a slight overestimate of the true objective on average; this bias is also present in the Dirichlet energy of Dodik et al. [2023]. We do not find either source of bias to be significant and leave derivation of practical fully-debiased estimates of the biharmonic energy to future work.*

We introduce a heuristic to address bleeding in evaluating the smoothness objective. Take $\mathbf{y}^\pm := \mathbf{y} \pm h\mathbf{v}$ to be a displaced sample used in evaluation of (18). When evaluating $\mathcal{N}_\theta(\mathbf{y}^\pm)$, we simply zero out the kernel k for those points \mathbf{x}_i that are not visible from \mathbf{y} .

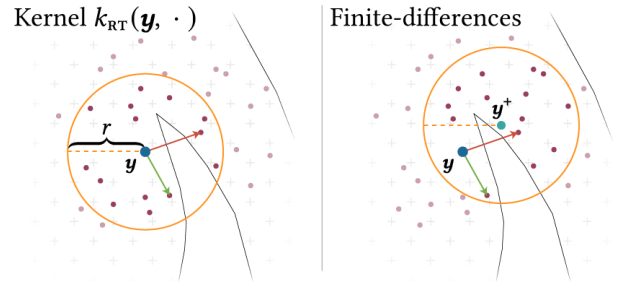


Fig. 7. The figure on the left visualizes our ray-tracing kernel k_{RT} . For an evaluation point \mathbf{y} , we look up all points within a radius r , and include into our estimate points which are visible from \mathbf{y} . Here we visualize a visible point with a green arrow pointing to it, and an occluded point with a red arrow. The figure on the right illustrates our visibility-aware finite-difference scheme. Our construction makes it so that the kernel estimate at \mathbf{y}^+ can only include points which are in a star-shaped neighborhood of \mathbf{y} .

6.3 Generalized-Winding Numbers Biharmonic Energy

We are able to apply our method to non-watertight geometries through an extension relying on robust methods popular in other parts of geometry processing.

In particular, we rely on generalized winding numbers [Jacobson et al. 2013] to perform robust inside-outside segmentation. For a watertight shape, the generalized winding number is a function $\text{gwn} : \mathbb{R}^d \rightarrow \mathbb{R}$, which equals 1 for all \mathbf{x} inside the shape and -1 for all \mathbf{x} outside of the shape. For an open shape, the generalized winding number smoothly varies from 1 to -1 as the percentage of the shape’s faces surrounding a point decreases.

We define two thresholds, gwn_l and gwn_h . Anything below gwn_l is considered completely outside the shape, and anything above gwn_h is completely inside. Our implementation uses $gwn_l = 0.1$ and $gwn_h = 0.4$.

We use gwn_l to reject points both when sampling our point cloud \mathcal{X} , as well as in each training batch. For all remaining points, we clip their generalized winding numbers above to gwn_h compute a weighted biharmonic energy as

$$\hat{\Delta}_h f(\mathbf{x}) = \frac{gwn(\mathbf{x}) - gwn_l}{gwn_h - gwn_l} \cdot \frac{-2f(\mathbf{x}) + f(\mathbf{x} + h\mathbf{Re}_0) + f(\mathbf{x} - h\mathbf{Re}_0)}{h^2}, \quad (19)$$

7 MULTISCALE OPTIMIZATION

Using a gradient descent method for optimizing smoothness energies incurs a trade-off. If we use a finite-difference step that is too small, we will have to wait longer for the boundary conditions to propagate inward. Since our formulation is nonconvex, this issue also can lead to local minima. If, however, we use a larger finite difference step size, we will get an overly blurry result (see Figure 8).

Inspired by multigrid methods and prior work on optimizing differential energies in neural fields [Li et al. 2023], we found that a multiscale approach offers an effective compromise. Specifically, we initiate our method by randomly sampling \mathcal{X} . We let the method optimize for a number of iterations before doubling the number of samples in \mathcal{X} . To initialize the new point cloud, we use N_θ to interpolate existing values f_i onto the new points. Additionally, we also interpolate Adam’s gradient moment estimates [Kingma and Ba 2014] in a similar fashion. As the radius of our kernel k and the finite-differences step size are related to the density of the point cloud (see Figure 9), they shrink as we up-sample the point-cloud.

The upsampling generally increases the absolute magnitude of the biharmonic energy as the interpolation kernel and finite-difference estimator progressively do less and less smoothing (see Figure 8). To stabilize the optimization, we progressively decrease the learning rate (see Section 8 for details). We demonstrate the effect of this strategy in Figure 8.

8 IMPLEMENTATION DETAILS

Our algorithm is primarily implemented in PyTorch [Paszke et al. 2019], with the exception of closest-point queries in Section 4.2 and geometry-aware radius queries in Section 5. For these, we provide our own low-level CUDA implementations.

The closest point-queries rely on the cuBQL library [Wald 2023], which internally builds a bounding-volume hierarchy over the boundary mesh. For the geometry-aware kernel queries, we first build an SPH hash-grid in CUDA, with hash-grid cell sizes equal to the kernel radius. For each query point, we loop over all of the points in the neighboring cells. If a point falls within the kernel radius, we trace a ray between it and the query point, as explained in Section 5. For the ray-tracing itself, we rely on hardware-acceleration via the Optix [Parker et al. 2010] and OWL [Wald 2020] libraries. In practice, this means that the kernel queries are implemented as *ray-generation* shaders in Optix parlance.

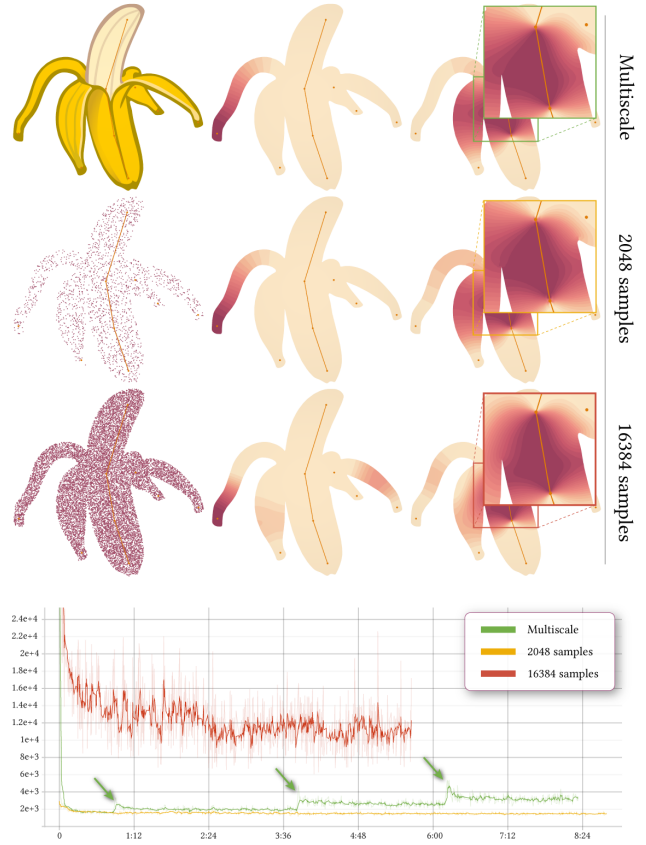


Fig. 8. A demonstration of the benefits of our multiscale optimization on the BANANA mesh (top left corner). The top row demonstrates the final results produced with our multiscale optimization strategy. The second row shows the results of optimizing with the a coarse point cloud of only 2048 samples. The optimization converges quickly, but the function is overly smooth near the control handles. Notably, this blurriness which has a global effect, with the middle handle extending too far into the leftmost handle. The following row shows that naïvely increasing the resolution results in slow convergence and possible local minima. Our multiscale approach does not suffer from these issues. The last row shows a time-vs.-loss plot of the three different strategies, with the green arrows pointing to the training iterations where the point-cloud is subdivided. The multiscale optimization results in a significantly lower loss compared to the largest point cloud.

We make the CUDA kernels interoperable with PyTorch by relying on nanobind [Jakob 2022]. We use the fast generalized winding numbers implementation from libigl [Jacobson and Panozzo 2017].

Before optimizing, we rescale meshes to fit into the $[0, 1]^d$ unit box. We generate \mathcal{X} by uniformly sampling the interior of the mesh, with an initial budget of 2^{11} points in 2D and 2^{13} points in 3D. If a mesh of the interior is unavailable, we rely on generalized winding numbers and perform rejection sampling until the target budget is reached. Our initial learning rate is set to 0.2.

We train for a total of 6000 steps, and double the size of \mathcal{X} a total of 3 times at regular intervals throughout the training. Every time

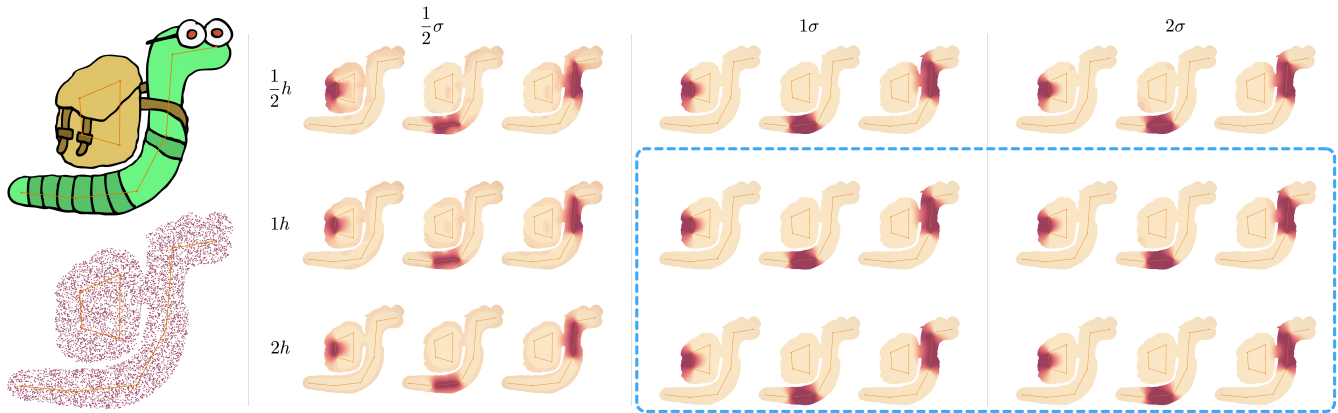


Fig. 9. Results of our ablation study. On the top, we show the effect of varying the kernel parameter σ , as well as the finite-difference step size, h . Making σ or h too small compared to the median spacing of points makes optimizing differential quantities difficult and leads to wrong results. Doubling the size of σ or h produces a similar result and would be viable choices of parameters, but it does unnecessarily increase the kernel look-up time.

	FISH	MUSHROOM	HAND	PENGUIN	GEAR	PIGGYBANK	BUNNY	SHIBA INU	SCORPION	BEAVER
Num. vertices	10.79k	11.59k	7.99k	13.44k	25.38k	23.84k	20.90k	3.97k	50.00k	97.11k
Num. faces	21.57k	23.17k	15.98k	26.88k	50.75k	31.12k	27.06k	1.95k	99.99k	173.37k
Uses GWN	No	No	No	No	Yes	Yes	Yes	No	Yes	Yes
Training time (min)	4.96	5.05	5.07	5.20	5.46	5.57	6.83	6.99	8.48	13.12
Inference time (ms)	68.18	51.10	57.50	67.58	101.00	86.39	91.27	52.17	149.58	1109.92

Table 1. Run-time statistics for the 3D meshes in this paper. We report the number of vertices and faces of the mesh, whether our computation used the generalized winding number for inside-outside testing, as well as the inference and training times. In general, meshes higher resolution meshes result in longer training times. As expected, having to evaluate the generalized winding number on the CPU also has an impact on the training time.

we upsample the representation, we lower the learning rate by a factor of 0.3.

We found it important to lower the β_2 parameter of Adam [Kingma and Ba 2014] to 0.8. A higher value of β_2 results in the optimizer slowing down if the gradient changes direction. This is useful in high-variance scenarios, but when optimizing variational energies, this is the opposite of what we want; in our scenario, gradients change directions often as boundary conditions propagate.

The sizes of the boundary condition parameters have been determined empirically. We set the value of the radii for the Neumann conditions as well as the Lagrange radius equal to the initial value of σ , but only update the radius of the Lagrange conditions as we upscale the point cloud.

9 RESULTS

To demonstrate the quality, robustness, and practicality of our skinning weights, we offer a thorough qualitative and quantitative validation of our method in Section 9.1, a discussion of the robustness of our method in Section 9.2, as well as comparisons

to previous work in Section 9.3. We discuss limitations and future work in Section 9.4.

We ran all of our experiments on a machine with an Intel i9-13900 CPU, 32 GB of memory, and an Nvidia GeForce RTX 4090. The comparison results for bounded biharmonic weights (BBW) [Jacobson et al. 2011] were generated in Matlab using the `gptoolbox` library [Jacobson et al. 2021], and for quasi-harmonic weights (QHW) [Wang and Solomon 2021] using the original authors' implementation. All of our deformations were produced using dual quaternion skinning [Kavan et al. 2008]. For consistency reasons, we use the same parameters for tetrahedralization software for all of our figures.

We offer training and inference timings for our method in Table 1. The biggest factor influencing our method's training runtime is the size of the boundary mesh. This is to be expected, as the size of the bounding volume hierarchy for the closest-point queries and the acceleration data structures for geometry-aware radius queries scale with the mesh size. Our implementation has not been tuned for performance, and we suspect that fully implementing the entire pipeline in CUDA—similarly to Instant NGP [Müller et al.

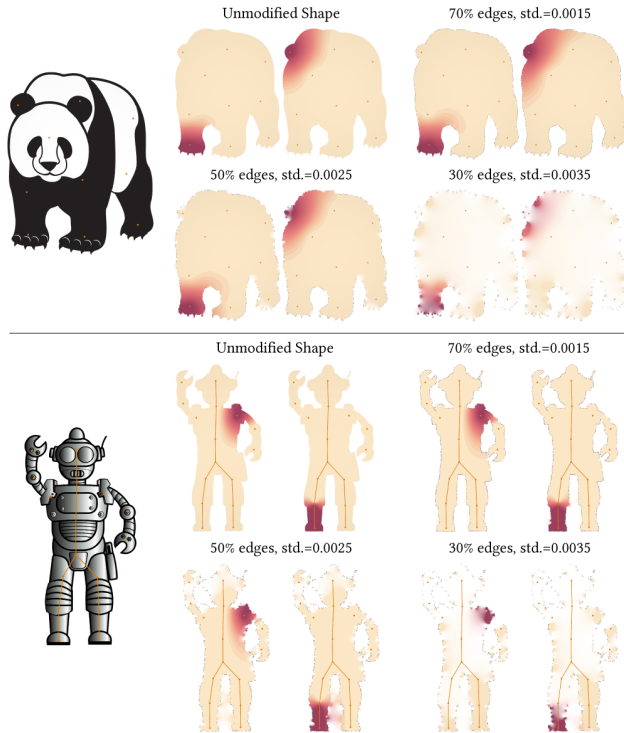


Fig. 10. Our method is effective even on heavily degraded geometric data. This figure shows the results of our method on a two shapes with progressively fewer boundary edges whose vertices have been randomly perturbed by adding progressively larger Gaussian noise.

2022] or Gaussian Splatting [Kerbl et al. 2023]—could further reduce computation time substantially.

9.1 Validation

Our method includes some hand-chosen parameters, most important of which are the number of points in \mathcal{X} , the size of σ , and the size of the finite-difference step h . To determine suitable values, we ran a series of ablation studies.

Figure 9 demonstrates the effects of varying σ and h . There is an inherent tension regarding the size of σ . On one hand, we want σ to be as small as possible to make radius queries as fast as possible and to avoid over-blurring the function. However, too small of a σ results in what is effectively a 1-nearest-neighbor estimator, which makes estimating differential quantities difficult. Hence, we set σ to the median distance to the fifth nearest neighbor in 2D and the ninth nearest neighbor in 3D. As shown in our ablation, this choice of σ makes it large enough to avoid any issues associated with a degenerate kernel estimator. At the same time, making it significantly larger than this value—while producing correct, if slightly blurry results—offers no benefit but increases the runtime.

In Figure 8, we ablate our multiscale optimization as compared to different sizes of \mathcal{X} . Too small of a point cloud results in an overly blurry representation, whereas too large of a point cloud results

in a higher loss, slower convergence and possible local minima. In comparison, our multiscale optimization consistently achieves the lowest loss.

9.2 Imperfect Data

Figures 1, 3, 10, 11, and 12 demonstrate the key contribution of our approach, its effectiveness on imperfect data. In general, solving variational problems on representations such as triangle soups is non-trivial, but despite heavy degradation, our method still produces meaningful solutions which can be used to produce smooth looking animations.

Figure 10 demonstrates the graceful degradation of our method inherited from the generalized winding number. Even in the presence of severe degradation, with 70% of the polygon edges removed, and the remaining ones randomly displaced, our method produces meaningful solutions.

We show an example of using our weights for animating a degraded version of the SCORPION mesh in Figure 1. Even without degradation, FEM-based algorithms struggle with this mesh. Using FTETWILD [Hu et al. 2020] with parameters consistent with Figure 3 results in a runtime of 1.6 hours and produces such a high-resolution tetrahedral mesh that both FEM methods we compared against run out of memory on our machine (see Figure 12 and Table 2). In comparison, our method takes 8.48 minutes for this mesh.

Practically, two important classes of shapes our method handles out-of-the-box are 3D scans obtained from computer vision pipelines (Figure 1), as well as virtual reality ribbon drawings created by e.g. SURFACEBRUSH [Rosales et al. 2019] (Figures 1 and 11). Both of these modalities produce non-watertight, self-intersecting meshes, which necessitate the use of slow and brittle tetrahedralization software.

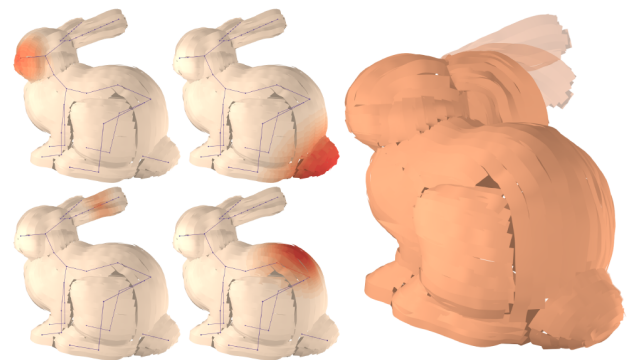


Fig. 11. Our method allows us to animate non-watertight, self-intersecting shapes, such as these virtual reality ribbon drawings created in SURFACEBRUSH [Rosales et al. 2019]. Despite the quality of the geometry, our method produces smooth-looking weights and animations.

9.3 Comparisons

Figure 13 compares skinning weights computed using our method with weights computed using bounded biharmonic weights (BBW) [Jacobson et al. 2011], as well as those computed using quasi-harmonic

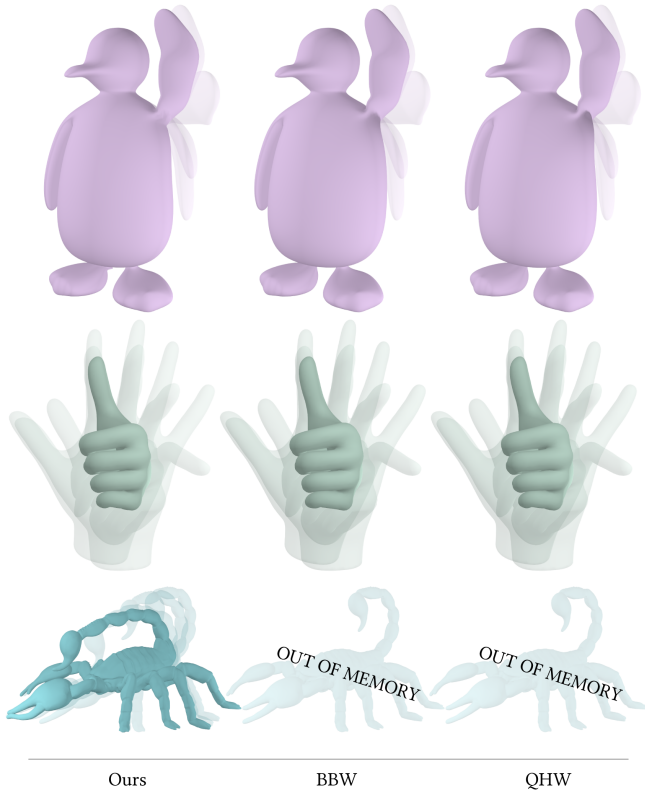


Fig. 12. We compare the deformations produced by our skinning weights with previous volumetric skinning weights methods: bounded biharmonic weights [Jacobson et al. 2013] (BBW) and quasi-harmonic weights (QHW) [Wang and Solomon 2021]. All methods produce similar results on simple geometries such as the PENGUIN and HAND meshes. However, on the more complicated SCORPION mesh, robust tetrahedralization software takes **1.6 hours**. It produces a tetrahedral mesh with a 70k vertices which is comparable to our 65k point-cloud points. Both BBW and QHW run out of RAM memory trying to process this mesh.

weights (QHW) [Wang and Solomon 2021]. As expected, all methods produce qualitatively similar weights functions but the setting is quite different: ours can work with a boundary mesh/polygon, while BBW requires filling the domain with elements by tri-/tet-meshing. Similar to past work and most applications of BBW, we found that solving the full BBW quadratic program was prohibitively slow on realistic examples and consequently dropped the partition-of-unity constraint, which was enforced *a posteriori* by dividing the weights by their sum pointwise. As for QHW [Wang and Solomon 2021], we set the width of their elliptic control handles to the same width as our σ at the end of training.

Figure 12 compares the animations produced by our method to those produced by BBW and QHW. Again, the results are nearly indistinguishable on simple meshes. The major difference is that our method does not require tetrahedralization software, nor does it need to deal with unpredictably large tetrahedral meshes it produces.

	HAND	PENGUIN	FISH	MUSHROOM	SCORPION
Vertices	16.10k	4.97k	58.10k	67.08	766.22k
Int. Vertices	7.24k	23.74k	28.41k	32.32k	91.96k
Tet. mesh (s)	0.51	1.88	2.36	2.875	5915.04
Ours (s)	303.22	311.86	298.31	302.22	504.67
BBW (s)	45.86	125.96	89.88	188.39	OOM
QHW (s)	12.10	12.77	7.16	15.13	OOM

Table 2. Statistics about the tetrahedral meshes produced by tet meshing software, as well as a run-time comparison of our method with BBW and QHW. While FEM-based methods are faster on well-behaved meshes, our method is able to produce results on meshes for which it was previously impossible to compute results.

We offer a quantitative comparison of the timings for the different methods in Table 2, as well as some statistics for the different tetrahedral meshes produced by tetrahedralization software. The HAND, PENGUIN, FISH, and MUSHROOM meshes are all relatively simple, well-behaved meshes, and could therefore be processed by tetgen [Si 2015]. This results in tetrahedral meshes with few interior vertices, that can be rapidly processed by downstream skinning weight solutions. Note that all of the tetrahedral meshes in this category have far fewer interior vertices than the 2^{16} scattered points that our algorithm has at the end of training. However, tetrahedralizing the SCORPION mesh produces an unexpectedly large mesh, resulting in both the FEM-based solvers running out of memory.

9.4 Limitations and Future Work

For a certain class of meshes, our method can produce minor artifacts due to the way we handle boundary conditions. Specifically, if a mesh feature is smaller than the boundary condition neighborhoods, our method can produce unexpected behaviors (see Figure 14). An interesting avenue for future work would be to automatically determine the sizes of the boundary condition neighborhoods based on the geometry of the shape.

An important avenue for future work would be to accelerate the method, so that its speed is closer to that of quasi-harmonic weights [Wang and Solomon 2021]. Methods such as [Wang and Solomon 2021], while using the Adam optimizer, also rely on preconditioning their solver as a way of accelerating the computation. Applying such solvers on problems involving geometric fields remains an interesting open problem. Another possible avenue is to design a way to reduce the sampling density of the Lagrangian representation in cases where the boundary geometry is not especially intricate. On the more practical side, fully-fused CUDA architectures have seen great success in adjacent domains [Kerbl et al. 2023; Müller et al. 2022], posing the obvious question of how much performance there is to be gained by adopting such an approach for our problem.

Lastly, our method is specifically tuned for the problem of finding bounded biharmonic weights, but one could imagine a more general

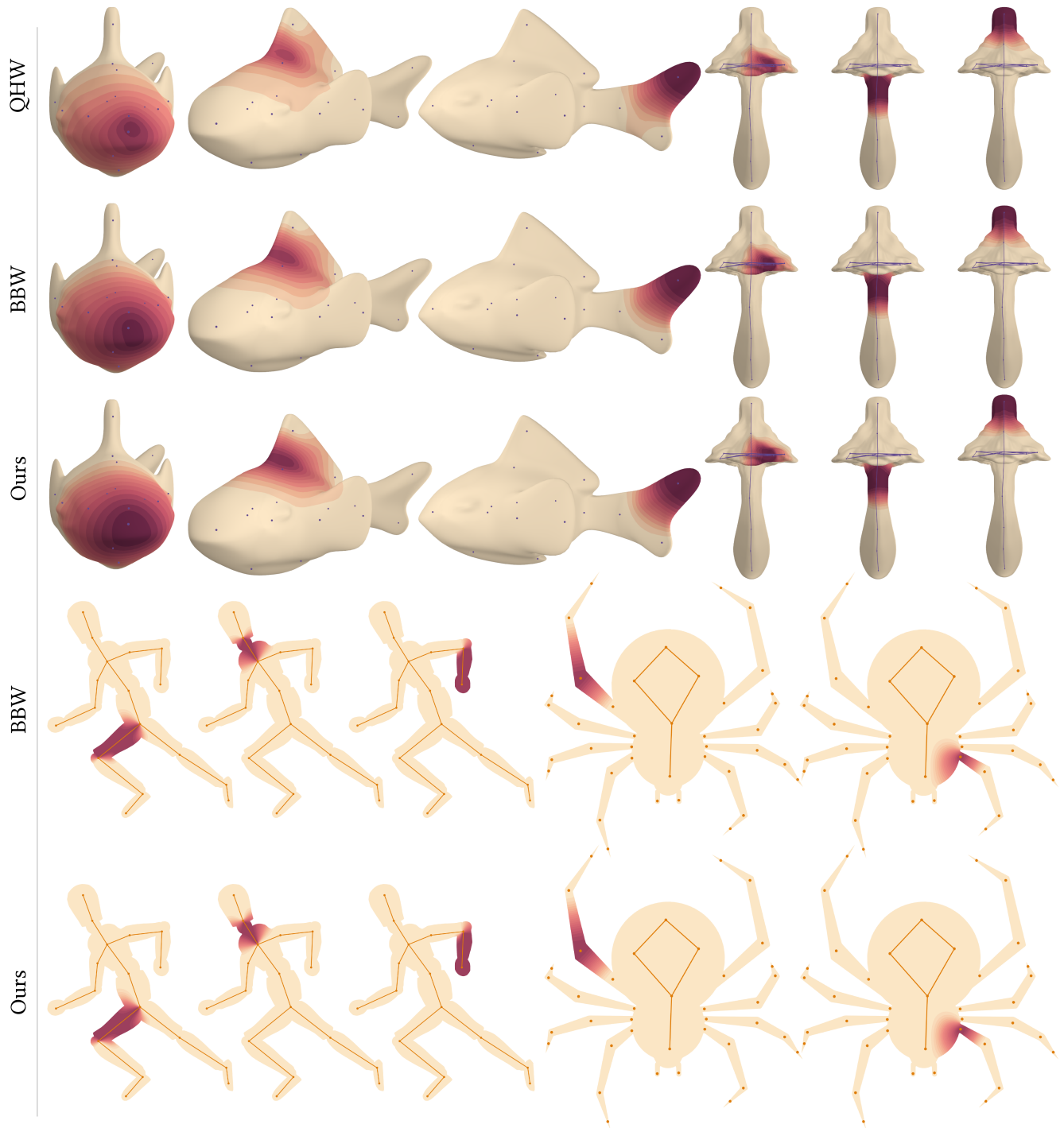


Fig. 13. Comparison of our results to quasi-harmonic weights QHW [Wang and Solomon 2021] and bounded biharmonic weights (BBW) [Jacobson et al. 2011]. QHW and BBW rely on tetrahedralization in 3D or triangulation in 2D, while our method requires only the boundary triangle mesh or polygon. All methods produce similar-looking weights as they are solving the same problem. Some minor differences are possible due to differences in discretization and enforcement of boundary conditions.

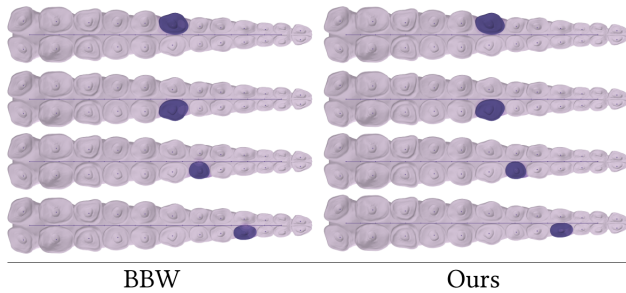


Fig. 14. Comparing the behavior of our method to that of bounded biharmonic weights on a particularly challenging scene. Not only is the TENTACLE mesh full of degenerate self-intersecting geometry, we have also adversarially placed the control handles such that the ε -radius of the Neumann boundary conditions intersects with the ε -radius of the Lagrange conditions. While most of the control handles are handled correctly by our method (e.g., top two rows), minor artifacts are visible in others. Nonetheless, robust tetrahedralization of the mesh using FTETWILD [Hu et al. 2020] not only produces visible artifacts, but also causes the handles to bleed through the geometry (bottom two rows). We recommend zooming in for better visibility.

framework for solving geometric problems using geometric fields. For example, we can imagine connections to the work of Sawhney and Crane [2020], where our method could be used either as a direct replacement, or—in cases where convergence guarantees are needed—as a control variate.

10 CONCLUSION

We propose a mesh-free approach to automatic computation of skinning weights. This is enabled by our geometric field representation of skinning weights, through which we may optimize the biharmonic energy without the need for finite elements or constraints. Our method enables skinning weights computation on previously challenging or even impossible shapes, such as those with open surfaces or triangle soups, while achieving quality comparable to that achieved by prior state-of-the-art approaches requiring volumetric meshes.

ACKNOWLEDGMENTS

We thank Yu Wang for helping us compare with quasi-harmonic weights, and to Enrique Rosales for the permission to use the PRGYBANK and BUNNY meshes.

The MIT Geometric Data Processing Group acknowledges the generous support of Army Research Office grants W911NF2010168 and W911NF2110293, of Air Force Office of Scientific Research award FA9550-19-1-031, of National Science Foundation grant CHS-1955697, from the CSAIL Systems that Learn program, from the MIT-IBM Watson AI Laboratory, from the Toyota-CSAIL Joint Research Center, from a gift from Adobe Systems, and from a Google Research Scholar award.

The MIT Scene Representation Group acknowledges the generous support of the National Science Foundation under Grant No. 2211259, of the Singapore DSTA under DST00OEI20300823 (New Representations for Vision), of the Intelligence Advanced Research Projects

Activity (IARPA) via Department of Interior/ Interior Business Center (DOI/IBC) under 140D0423C0075, of the Amazon Science Hub, and of IBM.

Oded Stein acknowledges the generous support of the SNF Early Postdoc Mobility fellowship.

REFERENCES

- Marc Alexa, Markus Gross, Mark Pauly, Hanspeter Pfister, Marc Stamminger, and Matthias Zwicker. 2004. Point-based computer graphics. In *ACM SIGGRAPH 2004 Course Notes* (Los Angeles, CA) (SIGGRAPH '04). Association for Computing Machinery, New York, NY, USA, 7–es. <https://doi.org/10.1145/1103900.1103907>
- Anonymous. 2024. Scaling physics-informed hard constraints with mixture-of-experts. In *The Twelfth International Conference on Learning Representations, submitted*. <https://openreview.net/forum?id=u3dX2CEIzb>
- MOSEK ApS. 2019. *The MOSEK optimization toolbox for MATLAB manual. Version 9.0*. <http://docs.mosek.com/9.0/toolbox/index.html>
- Seungbae Bang and Sung-Hee Lee. 2018. Spline interface for intuitive skinning weight editing. *ACM Transactions on Graphics (TOG)* 37, 5 (2018), 1–14.
- Ilya Baran and Jovan Popović. 2007. Automatic rigging and animation of 3d characters. *ACM Transactions on graphics (TOG)* 26, 3 (2007), 72–1–72–8.
- Mario Botsch and Leif Kobbelt. 2004. An intuitive framework for real-time freeform modeling. *ACM Transactions on Graphics (TOG)* 23, 3 (2004), 630–634.
- Honglin Chen, Rundi Wu, Eitan Grinspun, Changxi Zheng, and Peter Yichen Chen. 2023. Implicit Neural Spatial Representations for Time-dependent PDEs. In *International Conference on Machine Learning*.
- Simin Chen, Zhixiang Liu, Wenbo Zhang, and Jinkun Yang. 2024. A Hard-Constraint Wide-Body Physics-Informed Neural Network Model for Solving Multiple Cases in Forward Problems for Partial Differential Equations. *Applied Sciences* 14, 1 (2024).
- Xu Chen, Yufeng Zheng, Michael J Black, Otmar Hilliges, and Andreas Geiger. 2021. SNARF: Differentiable forward skinning for animating non-rigid neural implicit shapes. In *Proceedings of the IEEE/CVF International Conference on Computer Vision*. 11594–11604.
- Aditya Chetan, Guandao Yang, Zichen Wang, Steve Marschner, and Bharath Hariharan. 2023. Accurate Differential Operators for Hybrid Neural Fields. arXiv:2312.05984 [cs.CV]
- Ronald R. Coifman and Stéphane Lafon. 2006. Diffusion maps. *Applied and Computational Harmonic Analysis* 21, 1 (2006), 5–30. <https://doi.org/10.1016/j.acha.2006.04.006> Special Issue: Diffusion Maps and Wavelets.
- Lorenzo Diazzi, Daniele Panozzo, Amir Vaxman, and Marco Attene. 2023. Constrained Delaunay Tetrahedralization: A Robust and Practical Approach. *ACM Trans. Graph.* 42, 6, Article 181 (dec 2023), 15 pages. <https://doi.org/10.1145/3618352>
- Olivier Dionne and Martin de Lasa. 2013. Geodesic voxel binding for production character meshes. In *Proceedings of the 12th ACM SIGGRAPH/Eurographics Symposium on Computer Animation*. 173–180.
- Olivier Dionne and Martin de Lasa. 2014. Geodesic binding for degenerate character geometry using sparse voxelization. *IEEE Transactions on Visualization and Computer Graphics* 20, 10 (2014), 1367–1378.
- Franck Djeumou, Cyrus Neary, Eric Goubault, Sylvie Putot, and Ufuk Topcu. 2022. Neural Networks with Physics-Informed Architectures and Constraints for Dynamical Systems Modeling. arXiv:2109.06407 [cs.LG]
- Ana Dodik, Oded Stein, Vincent Sitzmann, and Justin Solomon. 2023. Variational Barycentric Coordinates. *ACM Transactions on Graphics* (2023). <https://doi.org/10.1145/3618403>
- Mark Gillespie, Nicholas Sharp, and Keenan Crane. 2021. Integer Coordinates for Intrinsic Geometry Processing. *ACM Trans. Graph.* 40, 6 (2021). <https://doi.org/10.1145/3478513.3480522>
- Robert A Gingold and Joseph J Monaghan. 1977. Smoothed particle hydrodynamics: theory and application to non-spherical stars. *Monthly Notices of the Royal Astronomical Society* 181, 3 (1977), 375–389.
- Amos Gropp, Lior Yariv, Niv Haim, Matan Atzmon, and Yaron Lipman. 2020. Implicit geometric regularization for learning shapes. *Proceedings of the 37th International Conference on Machine Learning* (2020).
- Henrik Halen and K Hayward. 2021. Global illumination based on surfels. In *Proc. ACM SIGGRAPH Symp. Interactive 3D Graph. Games*. 1399–1405.
- Yixin Hu, Tesseo Schneider, Xifeng Gao, Qingnan Zhou, Alec Jacobson, Denis Zorin, and Daniele Panozzo. 2019. TriWild: robust triangulation with curve constraints. *ACM Trans. Graph.* 38, 4, Article 52 (jul 2019), 15 pages. <https://doi.org/10.1145/3306346.3323011>
- Yixin Hu, Tesseo Schneider, Bolun Wang, Denis Zorin, and Daniele Panozzo. 2020. Fast Tetrahedral Meshing in the Wild. *ACM Trans. Graph.* 39, 4, Article 117 (July 2020), 18 pages. <https://doi.org/10.1145/3386569.3392385>
- Yixin Hu, Qingnan Zhou, Xifeng Gao, Alec Jacobson, Denis Zorin, and Daniele Panozzo. 2018. Tetrahedral Meshing in the Wild. *ACM Trans. Graph.* 37, 4, Article 60 (jul 2018), 14 pages. <https://doi.org/10.1145/3197517.3201353>

- Alec Jacobson et al. 2021. gptoolbox: Geometry Processing Toolbox. <http://github.com/alecjacobson/gptoolbox>.
- Alec Jacobson, Ilya Baran, Jovan Popović, and Olga Sorkine. 2011. Bounded Biharmonic Weights for Real-Time Deformation. *ACM Transactions on Graphics (proceedings of ACM SIGGRAPH)* 30, 4 (2011), 78:1–78:8.
- Alec Jacobson, Zhigang Deng, Ladislav Kavan, and J. P. Lewis. 2014. Skinning: Real-Time Shape Deformation (Full Text Not Available). In *ACM SIGGRAPH 2014 Courses (Vancouver, Canada) (SIGGRAPH '14)*. Association for Computing Machinery, New York, NY, USA, Article 24, 1 pages. <https://doi.org/10.1145/2614028.2615427>
- Alec Jacobson, Ladislav Kavan, and Olga Sorkine. 2013. Robust Inside-Outside Segmentation using Generalized Winding Numbers. *ACM Trans. Graph.* 32, 4 (2013).
- Alec Jacobson and Daniele Panozzo. 2017. libigl: prototyping geometry processing research in C++. In *SIGGRAPH Asia 2017 Courses (Bangkok, Thailand) (SA '17)*. Association for Computing Machinery, New York, NY, USA, Article 11, 172 pages. <https://doi.org/10.1145/3134472.3134497>
- Alec Jacobson, Elif Tosun, Olga Sorkine, and Denis Zorin. 2010. Mixed finite elements for variational surface modeling. In *Computer graphics forum*, Vol. 29. Wiley Online Library, 1565–1574.
- Alec Jacobson, Tino Weinkauff, and Olga Sorkine. 2012a. Smooth Shape-Aware Functions with Controlled Extrema. *Computer Graphics Forum (proceedings of EUROGRAPHICS/ACM SIGGRAPH Symposium on Geometry Processing)* 31, 5 (2012), 1577–1586.
- Alec Jacobson, Tino Weinkauff, and Olga Sorkine. 2012b. Smooth shape-aware functions with controlled extrema. In *Computer Graphics Forum*, Vol. 31. Wiley Online Library, 1577–1586.
- Wenzel Jakob. 2022. nanobind: tiny and efficient C++/Python bindings. <https://github.com/wjakob/nanobind>.
- Doug L James and Christopher D Twigg. 2005. Skinning mesh animations. *ACM Transactions on Graphics (TOG)* 24, 3 (2005), 399–407.
- Timothy Jeruzalski, David IW Levin, Alec Jacobson, Paul Lalonde, Mohammad Norouzi, and Andrea Tagliasacchi. 2020. NiLBS: Neural inverse linear blend skinning. *arXiv:2004.05980* (2020).
- Pushkar Joshi, Mark Meyer, Tony DeRose, Brian Green, and Tom Sanocki. 2007. Harmonic coordinates for character articulation. *ACM Transactions on Graphics (TOG)* 26, 3 (2007), 71–1–71–9.
- Yash Kant, Aliaksandr Siarohin, Riza Alp Guler, Menglei Chai, Jian Ren, Sergey Tulyakov, and Igor Gilitschenski. 2023. Invertible Neural Skinning. In *Proceedings of the IEEE/CVF Conference on Computer Vision and Pattern Recognition*. 8715–8725.
- Ladislav Kavan, Steven Collins, Jiri Zara, and Carol O’Sullivan. 2008. Geometric Skinning with Approximate Dual Quaternion Blending. *ACM Trans. Graph.* 27, 4 (2008), 105.
- Ladislav Kavan, Peter-Pike Sloan, and Carol O’Sullivan. 2010. Fast and efficient skinning of animated meshes. In *Computer Graphics Forum*, Vol. 29. Wiley Online Library, 327–336.
- Bernhard Kerbl, Georgios Kopanas, Thomas Leimkühler, and George Drettakis. 2023. 3D Gaussian Splatting for Real-Time Radiance Field Rendering. *ACM Transactions on Graphics* 42, 4 (2023).
- Diederik P Kingma and Jimmy Ba. 2014. Adam: A method for stochastic optimization. *arXiv:1412.6980* (2014).
- Muhammed Kocabas, Jen-Hao Rick Chang, James Gabriel, Oncel Tuzel, and Anurag Ranjan. 2023. HUGS: Human gaussian splats. *arXiv:2311.17910* (2023).
- Binh Huy Le and Zhigang Deng. 2012. Smooth skinning decomposition with rigid bones. *ACM Transactions on Graphics (TOG)* 31, 6 (2012), 1–10.
- Binh Huy Le and Zhigang Deng. 2014. Robust and accurate skeletal rigging from mesh sequences. *ACM Transactions on Graphics (TOG)* 33, 4 (2014), 1–10.
- Binh Huy Le and JP Lewis. 2019. Direct delta mush skinning and variants. *ACM Trans. Graph.* 38, 4 (2019), 113–1.
- Peizhuo Li, Kfir Aberman, Rana Hanocka, Libin Liu, Olga Sorkine-Hornung, and Baoquan Chen. 2021. Learning skeletal articulations with neural blend shapes. *ACM Transactions on Graphics (TOG)* 40, 4 (2021), 1–15.
- Zhaoshuo Li, Thomas Müller, Alex Evans, Russell H Taylor, Mathias Unberath, Mingyu Liu, and Chen-Hsuan Lin. 2023. Neuralangelo: High-Fidelity Neural Surface Reconstruction. In *IEEE Conference on Computer Vision and Pattern Recognition (CVPR)*.
- Zhouyincheng Liao, Vladislav Golyanik, Marc Habermann, and Christian Theobalt. 2023. VINECS: Video-based Neural Character Skinning. *arXiv:2307.00842* (2023).
- Lijuan Liu, Youyi Zheng, Di Tang, Yi Yuan, Changjie Fan, and Kun Zhou. 2019. Neuroskinning: Automatic skin binding for production characters with deep graph networks. *ACM Transactions on Graphics (ToG)* 38, 4 (2019), 1–12.
- Songming Liu, Hao Zhongkai, Chengyang Ying, Hang Su, Jun Zhu, and Ze Cheng. 2022. A Unified Hard-Constraint Framework for Solving Geometrically Complex PDEs. In *Advances in Neural Information Processing Systems*, Vol. 35. 20287–20299.
- Lu Lu, Raphael Pestourie, Wenjie Yao, Zhicheng Wang, Francesc Verdugo, and Steven G. Johnson. 2021. Physics-informed neural networks with hard constraints for inverse design. *arXiv:2102.04626* [physics.comp-ph]
- Leon B Lucy. 1977. A numerical approach to the testing of the fission hypothesis. *Astronomical Journal* 82 (1977), 1013–1024.
- Jing Ma and Dongliang Zhang. 2023. TARig: Adaptive template-aware neural rigging for humanoid characters. *Computers & Graphics* (2023).
- Qianli Ma, Jinlong Yang, Michael J Black, and Siyu Tang. 2022. Neural Point-based Shape Modeling of Humans in Challenging Clothing. In *International Conference on 3D Vision (3DV)*. IEEE, 679–689.
- N. Magnenat-Thalmann, A. Laperrrière, and D. Thalmann. 1988. Joint-Dependent Local Deformations for Hand Animation and Object Grasping. In *Proceedings of Graphics Interface '88* (Edmonton, Alberta, Canada) (GI '88). Canadian Man-Computer Communications Society, Toronto, Ontario, Canada, 26–33. <http://graphicsinterface.org/wp-content/uploads/gi1988-4.pdf>
- Zander Majercik, Jean-Philippe Guertin, Derek Nowrouzezahrai, and Morgan McGuire. 2019. Dynamic Diffuse Global Illumination with Ray-Traced Irradiance Fields. *Journal of Computer Graphics Techniques (JCGT)* 8, 2 (5 June 2019), 1–30. <http://jcgct.org/published/0008/02/01/>
- Bailey Miller, Rohan Sawhney, Keenan Crane, and Ioannis Gkioulekas. 2023. Boundary Value Caching for Walk on Spheres. *ACM Trans. Graph.* 42, 4 (2023).
- Arvind T. Mohan, Nicholas Lubbers, Misha Chertkov, and Daniel Livescu. 2023. Embedding hard physical constraints in neural network coarse-graining of three-dimensional turbulence. *Phys. Rev. Fluids* 8 (2023), 17 pages. Issue 1.
- Albert Mosella-Montoro and Javier Ruiz-Hidalgo. 2022. SkinningNet: Two-stream graph convolutional neural network for skinning prediction of synthetic characters. In *Proceedings of the IEEE/CVF Conference on Computer Vision and Pattern Recognition*. 18593–18602.
- Thomas Müller, Alex Evans, Christoph Schied, and Alexander Keller. 2022. Instant Neural Graphics Primitives with a Multiresolution Hash Encoding. *ACM Trans. Graph.* 41, 4, Article 102 (July 2022), 15 pages. <https://doi.org/10.1145/3528223.3530127>
- E. A. Nadaraya. 1964. On Estimating Regression. *Theory of Probability & Its Applications* 9, 1 (1964), 141–142. <https://doi.org/10.1137/1109020> [arXiv:https://doi.org/10.1137/1109020](https://arxiv.org/abs/10.1137/1109020)
- Xuming Ouyang and Cunguang Feng. 2020. AutoSkin: Skeleton-based Human Skinning with Deep Neural Networks. In *Journal of Physics: Conference Series*, Vol. 1550. IOP Publishing, 032163.
- Xiaoyu Pan, Jiancong Huang, Jiaming Mai, He Wang, Honglin Li, Tongkui Su, Wenjun Wang, and Xiaogang Jin. 2021. HeterSkinNet: A Heterogeneous Network for Skin Weights Prediction. In *Proceedings of the ACM on Computer Graphics and Interactive Techniques*, Vol. 4. Association for Computing Machinery.
- Steven G. Parker, James Bigler, Andreas Dietrich, Heiko Friedrich, Jared Hoberock, David Luebke, David McAllister, Morgan McGuire, Keith Morley, Austin Robison, and Martin Stich. 2010. OptiX: A General Purpose Ray Tracing Engine. *ACM Transactions on Graphics* (August 2010).
- Adam Paszke, Sam Gross, Francisco Massa, Adam Lerer, James Bradbury, Gregory Chanan, Trevor Killeen, Zeming Lin, Natalia Gimelshein, Luca Antiga, Alban Desmaison, Andreas Kopf, Edward Yang, Zachary DeVito, Martin Raison, Alykhan Tejani, Sasank Chilamkurthy, Benoit Steiner, Lu Fang, Junjie Bai, and Soumith Chintala. 2019. PyTorch: An Imperative Style, High-Performance Deep Learning Library. In *Advances in Neural Information Processing Systems* 32. Curran Associates, Inc., 8024–8035. <http://papers.neurips.cc/paper/9015-pytorch-an-imperative-style-high-performance-deep-learning-library.pdf>
- Mark Pauly, Richard Keiser, Leif P. Kobbelt, and Markus Gross. 2003. Shape modeling with point-sampled geometry. *ACM Trans. Graph.* 22, 3 (jul 2003), 641–650. <https://doi.org/10.1145/882262.882319>
- Matt Pharr, Wenzel Jakob, and Greg Humphreys. 2016. *Physically Based Rendering: From Theory to Implementation (3rd ed.)* (3rd ed.). Morgan Kaufmann Publishers Inc., San Francisco, CA, USA. 1266 pages.
- Maziar Raissi, Paris Perdikaris, and George E Karniadakis. 2019. Physics-informed neural networks: A deep learning framework for solving forward and inverse problems involving nonlinear partial differential equations. *J. Comput. Phys.* 378 (2019), 686–707.
- Ruben Rodriguez-Torrado, Pablo Ruiz, Luis Cueto-Felgueroso, Michael Cerny Green, Tyler Friesen, Sebastien Matringe, and Julian Togelius. 2021. Physics-informed attention-based neural network for solving non-linear partial differential equations. *arXiv:2105.07898* [cs.LG]
- Enrique Rosales, Jafet Rodriguez, and Alla Sheffer. 2019. SurfaceBrush: From Virtual Reality Drawings to Manifold Surfaces. *ACM Transaction on Graphics* 38, 4 (2019). <https://doi.org/10.1145/3306346.3322970>
- Rohan Sawhney and Keenan Crane. 2020. Monte Carlo Geometry Processing: A Grid-Free Approach to PDE-Based Methods on Volumetric Domains. *ACM Trans. Graph.* 39, 4 (2020).
- Rohan Sawhney, Bailey Miller, Ioannis Gkioulekas, and Keenan Crane. 2023. Walk on Stars: A Grid-Free Monte Carlo Method for PDEs with Neumann Boundary Conditions. *ACM Trans. Graph.* 42, 4 (2023).
- Rohan Sawhney, Dario Seyb, Wojciech Jarosz, and Keenan Crane. 2022. Grid-Free Monte Carlo for PDEs with Spatially Varying Coefficients. *ACM Trans. Graph.* XX, X (2022).

- Nicholas Sharp and Keenan Crane. 2020a. A laplacian for nonmanifold triangle meshes. In *Computer Graphics Forum*, Vol. 39. Wiley Online Library, 69–80.
- Nicholas Sharp and Keenan Crane. 2020b. You Can Find Geodesic Paths in Triangle Meshes by Just Flipping Edges. *ACM Trans. Graph.* 39, 6 (2020).
- Nicholas Sharp, Mark Gillespie, and Keenan Crane. 2021. Geometry Processing with Intrinsic Triangulations. (2021).
- Hang Si. 2015. TetGen, a Delaunay-Based Quality Tetrahedral Mesh Generator. *ACM Trans. Math. Softw.* 41, 2, Article 11 (feb 2015), 36 pages. <https://doi.org/10.1145/2629697>
- Vincent Sitzmann, Julien N.P. Martel, Alexander W. Bergman, David B. Lindell, and Gordon Wetzstein. 2020. Implicit Neural Representations with Periodic Activation Functions. In *Proceedings of the Conference on Neural Information Processing Systems*.
- Justin Solomon, Amir Vaxman, and David Bommes. 2017. Boundary element octahedral fields in volumes. *ACM Transactions on Graphics (TOG)* 36, 4 (2017), 1.
- Oded Stein, Eitan Grinspun, Max Wardetzky, and Alec Jacobson. 2018. Natural boundary conditions for smoothing in geometry processing. *ACM Transactions on Graphics (TOG)* 37, 2 (2018), 1–13.
- Ryusuke Sugimoto, Christopher Batty, and Toshiya Hachisuka. 2022. Surface-Only Dynamic Deformables using a Boundary Element Method. In *Computer Graphics Forum*, Vol. 41. Wiley Online Library, 75–86.
- N. Sukumar and Ankit Srivastava. 2022. Exact imposition of boundary conditions with distance functions in physics-informed deep neural networks. *Computer Methods in Applied Mechanics and Engineering* 389 (2022), 114333.
- J-M Thiery and Elmar Eisemann. 2018. ARAPLBS: Robust and efficient elasticity-based optimization of weights and skeleton joints for linear blend skinning with parametrized bones. In *Computer Graphics Forum*, Vol. 37. Wiley Online Library, 32–44.
- Elif Tosun. 2008. *Geometric modeling using high-order derivatives*. Ph. D. Dissertation. New York University.
- Jane Tournois, Noura Faraj, Jean-Marc Thiery, and Tamy Boubekeur. 2024. Tetrahedral Remeshing. In *CGAL User and Reference Manual* (5.6.1 ed.). CGAL Editorial Board. <https://doc.cgal.org/5.6.1/Manual/packages.html#PkgTetrahedralRemeshing>
- Ingo Wald. 2020. OWL - A Productivity Library for OptiX. <http://owl-project.github.io>
- Ingo Wald. 2023. cuBQL - A CUDA BVH Build and Query Library. <http://github.com/ingowald/cuBQL>
- Kevin Wampler. 2016. Fast and reliable example-based mesh IK for stylized deformations. *ACM Transactions on Graphics (TOG)* 35, 6 (2016), 1–12.
- Yu Wang, Alec Jacobson, Jernej Barbič, and Ladislav Kavan. 2015. Linear Subspace Design for Real-Time Shape Deformation. *ACM Trans. Graph.* 34, 4, Article 57 (2015), 11 pages.
- Yu Wang and Justin Solomon. 2021. Fast quasi-harmonic weights for geometric data interpolation. *ACM Transactions on Graphics (TOG)* 40, 4 (2021), 1–15.
- Geoffrey S. Watson. 1964. Smooth Regression Analysis. *Sankhyā: The Indian Journal of Statistics, Series A (1961-2002)* 26, 4 (1964), 359–372. <http://www.jstor.org/stable/25049340>
- Jane Wu, Zhenglin Geng, Hui Zhou, and Ronald Fedkiw. 2020. Skinning a parameterization of three-dimensional space for neural network cloth. *arXiv:2006.04874* (2020).
- Shangzhe Wu, Ruining Li, Tomas Jakab, Christian Ruppert, and Andrea Vedaldi. 2023. MagicPony: Learning articulated 3d animals in the wild. In *Proceedings of the IEEE/CVF Conference on Computer Vision and Pattern Recognition*. 8792–8802.
- Yiheng Xie, Towaki Takikawa, Shunsuke Saito, Or Litany, Shiqin Yan, Numair Khan, Federico Tombari, James Tompkin, Vincent Sitzmann, and Srinath Sridhar. 2022. Neural fields in visual computing and beyond. In *Computer Graphics Forum*, Vol. 41. Wiley Online Library, 641–676.
- Zhan Xu, Yang Zhou, Evangelos Kalogerakis, Chris Landreth, and Karan Singh. 2020. RigNet: neural rigging for articulated characters. *ACM Transactions on Graphics (TOG)* 39, 4 (2020), 58–1.
- Ze Yang, Shenlong Wang, Sivabalan Manivasagam, Zeng Huang, Wei-Chiu Ma, Xinchun Yan, Ersin Yumer, and Raquel Urtasun. 2021. S3: Neural shape, skeleton, and skinning fields for 3d human modeling. In *Proceedings of the IEEE/CVF Conference on Computer Vision and Pattern Recognition*. 13284–13293.
- Fangcheng Zhong, Kyle Fogarty, Param Hanji, Tianhao Wu, Alejandro Sztrajman, Andrew Spielberg, Andrea Tagliasacchi, Petra Bosilj, and Cengiz Oztireli. 2023. Neural Fields with Hard Constraints of Arbitrary Differential Order. *arXiv:2306.08943 [cs.LG]*